UMass Chan Medical School
eScholarship@UMassChan

COVID-19 Publications by UMass Chan Authors

2021-12-16

High-affinity, neutralizing antibodies to SARS-CoV-2 can be made without T follicular helper cells

Jennifer S. Chen
Yale University

Et al.

Let us know how access to this document benefits you.
Follow this and additional works at: https://escholarship.umassmed.edu/covid19

Part of the Immunology of Infectious Disease Commons, Infectious Disease Commons, Microbiology Commons, and the Virus Diseases Commons

Repository Citation
Chen JS, Uthaman G, Wilen CB, Eisenbarth SC. (2021). High-affinity, neutralizing antibodies to SARS-CoV-2 can be made without T follicular helper cells. COVID-19 Publications by UMass Chan Authors. https://doi.org/10.1126/sciimmunol.abl5652. Retrieved from https://escholarship.umassmed.edu/covid19/335

Creative Commons License

This work is licensed under a Creative Commons Attribution 4.0 License.
This material is brought to you by eScholarship@UMassChan. It has been accepted for inclusion in COVID-19 Publications by UMass Chan Authors by an authorized administrator of eScholarship@UMassChan. For more information, please contact Lisa.Palmer@umassmed.edu.

Cite as: J. S. Chen *et al.*, *Sci. Immunol.* 10.1126/sciimmunol.abl5652 (2021).

CORONAVIRUS

High-affinity, neutralizing antibodies to SARS-CoV-2 can be made without T follicular helper cells

Jennifer S. Chen[1,2], Ryan D. Chow[3,4], Eric Song[2], Tianyang Mao[2], Benjamin Israelow[2,5], Kathy Kamath[6], Joel Bozekowski[6], Winston A. Haynes[6], Renata B. Filler[1,2], Bridget L. Menasche[1,2], Jin Wei[1,2], Mia Madel Alfajaro[1,2], Wenzhi Song[2], Lei Peng[3,4], Lauren Carter[7], Jason S. Weinstein[8], Uthaman Gowthaman[9], Sidi Chen[3,4], Joe Craft[2], John C. Shon[6], Akiko Iwasaki[2,10], Craig B. Wilen[1,2]*, Stephanie C. Eisenbarth[1,2]*

[1]Department of Laboratory Medicine, Yale University School of Medicine; New Haven, CT, USA. [2]Department of Immunobiology, Yale University School of Medicine; New Haven, CT, USA. [3]Department of Genetics, Yale University School of Medicine; New Haven, CT, USA. [4]Systems Biology Institute, Yale University; West Haven, CT, USA. [5]Department of Internal Medicine, Section of Infectious Diseases, Yale University School of Medicine; New Haven, CT, USA. [6]Serimmune, Inc.; Goleta, CA, USA. [7]Institute for Protein Design, University of Washington; Seattle, WA, USA. [8]Center for Immunity and Inflammation, Rutgers New Jersey Medical School; Newark, NJ, USA. [9]Deparment of Pathology, University of Massachusetts Medical School; Worcester, MA, USA. [10]Howard Hughes Medical Institute; Chevy Chase, MD, USA.

*Corresponding authors. Email: craig.wilen@yale.edu (CBW), stephanie.eisenbarth@yale.edu (SCE)

T follicular helper (Tfh) cells are the conventional drivers of protective, germinal center (GC)-based antiviral antibody responses. However, loss of Tfh cells and GCs has been observed in patients with severe COVID-19. As T cell-B cell interactions and immunoglobulin class switching still occur in these patients, non-canonical pathways of antibody production may be operative during SARS-CoV-2 infection. We found that both Tfh-dependent and -independent antibodies were induced against SARS-CoV-2 infection, SARS-CoV-2 vaccination, and influenza A virus infection. Even though Tfh-independent antibodies to SARS-CoV-2 had evidence of reduced somatic hypermutation, they were still high-affinity, durable, and reactive against diverse spike-derived epitopes and were capable of neutralizing both homologous SARS-CoV-2 and the B.1.351 (beta) variant of concern. Indeed, we found by epitope mapping and BCR sequencing that Tfh cells focused the B cell response and therefore, in the absence of Tfh cells, a more diverse clonal repertoire was maintained. These data support an alternative pathway for the induction of B cell responses during viral infection that enables effective, neutralizing antibody production to complement traditional GC-derived antibodies that might compensate for GCs damaged by viral inflammation.

INTRODUCTION

Antibodies mediate protection against severe acute respiratory syndrome coronavirus 2 (SARS-CoV-2), the causative agent of the coronavirus disease 2019 (COVID-19) pandemic (*1*). T follicular helper (Tfh) cells are the conventional drivers of protective antibody responses, as they support immunoglobulin class switching, germinal center (GC)-based affinity maturation, and long-lived humoral immunity (*2*). Indeed, multiple studies have reported a correlation between circulating Tfh (cTfh) cells – in particular, type 1 $CXCR3^+CCR6^-$ cTfh cells – and neutralizing antibody titers in COVID-19 patients (*3*). While there have been mixed findings on the association of Tfh cells with disease severity, several groups have observed an absence of Tfh cells and GCs in severely ill patients (*4*–*7*). Despite a loss of Tfh cells and GC structures, T cell-B cell interactions and antibody class switching still occur in the secondary lymphoid organs of these patients (*6*). Findings of enhanced extrafollicular B cell responses associated with severe disease further suggest that non-canonical pathways of antibody production may be operative in these individuals (*6*, *8*). However, a causal relationship between antibody provenance and disease severity cannot be established by existing human studies. Thus, it remains unclear whether antibodies produced through non-canonical pathways without Tfh cell help are also protective against SARS-CoV-2.

No study has evaluated the requirement for Tfh cells in antibody production to SARS-CoV-2. Previous work with a related coronavirus, SARS-CoV-1, has shown that $CD4^+$ T cells are required for neutralizing antibody production (*9*), but the necessary $CD4^+$ T cell subset has not been identified. For other viruses, as well as bacteria, Tfh cells are thought to be required for class-switched, pathogen-specific antibody production, especially at later timepoints (*10*–*18*). In contrast, different studies have found conflicting results on the requirement of Tfh cells during vaccination in mice. Certain vaccine strategies induce robust Tfh-independent antibody responses, though of lower affinity (*19*, *20*), while other strategies fail to induce durable, class-switched, or high-affinity antibodies in mice with Tfh cell deficiency or dysfunction (*11*, *21*–*23*). In humans though, cTfh cell populations in the blood correlate with the response to influenza vaccination (*24*, *25*).

Downloaded from https://www.science.org at University of Massachusetts Worcester on January 12, 2022

Taken together, while non-Tfh CD4$^+$ T cells can promote effective antibodies in certain contexts, protective anti-pathogen humoral immunity is largely thought to be Tfh cell-dependent.

We therefore directly tested whether non-Tfh CD4$^+$ T cells could compensate for Tfh cell loss in severe COVID-19, and perhaps during acute viral infection in general, by promoting class-switched antibodies. We also sought to compare the Tfh-independent antibody response to SARS-CoV-2 infection with that induced by mRNA vaccination. Based on prior work, we hypothesized that antibodies induced through such non-canonical mechanisms would be lower in quantity and quality. To test this, we characterized the titer, isotype, longevity, affinity, epitope reactivity, and function of antibodies to SARS-CoV-2 infection from Tfh-deficient mice. We also examined antibody titers and isotypes following SARS-CoV-2 vaccination and influenza A virus infection. Both Tfh cells and non-Tfh CD4$^+$ T cells promoted class-switched antibodies to SARS-CoV-2 infection, SARS-CoV-2 vaccination, and influenza A virus. Contrary to our expectations, Tfh-independent antibodies to SARS-CoV-2 were durable and remarkably high-affinity, though B cell receptors from Tfh-deficient mice demonstrated impaired somatic hypermutation and mutation selection. Tfh-independent antibodies were also broadly reactive against diverse SARS-CoV-2 epitopes and effective at neutralizing both homologous and heterologous viruses. Thus, our study supports a paradigm for T cell-driven antibody responses to viruses in which multiple types of CD4$^+$ T cells in lymphoid organs coordinate the humoral response to viruses. This understanding of T cell-B cell interaction could aid in approaches to develop effective protection against SARS-CoV-2 as well as other viruses.

RESULTS

SARS-CoV-2 infection and vaccination induce Tfh-dependent and -independent antibodies

To study the cellular pathways that promote antibody production to SARS-CoV-2, we used mice that lack different CD4$^+$ T cell subsets. *Bcl6*$^{fl/fl}$*Cd4*^{Cre} mice are a well-established model of Tfh cell deficiency due to deletion of the Tfh lineage-defining transcription factor BCL6 (*17*, *22*, *26*). *Ciita*$^{-/-}$ mice lack all CD4$^+$ T cells due to loss of MHC class II expression (*27*). As SARS-CoV-2 is unable to efficiently interact with mouse ACE2, we utilized two models of human ACE2 (hACE2) overexpression: intratracheal administration of AAV-hACE2, which leads to hACE2 expression in the respiratory tract, and K18-hACE2 transgenic mice, which express hACE2 in epithelial cells (*28*–*30*).

We first assessed the cellular responses to SARS-CoV-2 infection in AAV-hACE2 mice. Two weeks after AAV-hACE2 transduction, we infected mice intranasally with SARS-CoV-2 (isolate USA-WA1/2020). At 14 days post infection (dpi), PD-1^{hi}CXCR5^{hi} Tfh cells were efficiently deleted in the mediastinal LN (medLN) of AAV-hACE2 *Bcl6*$^{fl/fl}$*Cd4*^{Cre} mice (Fig. S1, A to C). Consistent with the loss of Tfh cells, GC B cells were severely impaired, and plasmablast formation was reduced (Fig. S1, D to H). Yet, viral burden in the lungs of AAV-hACE2 *Bcl6*$^{fl/fl}$ and *Bcl6*$^{fl/fl}$*Cd4*^{Cre} mice was similar at 7 dpi (Fig. S1I). To examine the cellular architecture of the medLN in mice lacking Tfh cells, we performed immunofluorescence on K18-hACE2 *Bcl6*$^{fl/fl}$ and *Bcl6*$^{fl/fl}$*Cd4*^{Cre} mice at 14 dpi. K18-hACE2 *Bcl6*$^{fl/fl}$ medLN exhibited robust GC formation, with large clusters of activated (GL7$^+$) B cells colocalizing with CD35$^+$ follicular dendritic cell (FDC) networks and infiltrated by T cells (Fig. S2A), presumably Tfh cells. In contrast, K18-hACE2 *Bcl6*$^{fl/fl}$*Cd4*^{Cre} medLN displayed a few small clusters of GL7$^+$ cells that co-localized with sparse FDC networks but lacked T cells (Fig. S2B), congruent with the absence of Tfh cells. As GL7 is a marker of activated lymphocytes, including those outside of GCs, these rare cellular aggregates lacking T cells could represent sites of T-independent antigen-driven B cell stimulation.

We next determined the humoral responses to SARS-CoV-2 infection in AAV-hACE2 mice at 14 dpi (Fig. 1A). *Bcl6*$^{fl/fl}$ mice produced high levels of spike (S)-specific IgG antibodies (Fig. 1B). While *Bcl6*$^{fl/fl}$*Cd4*^{Cre} mice had reduced levels of S-specific IgG, they still produced substantially more compared to *Ciita*$^{-/-}$ mice. Among IgG subclasses, S-specific IgG1 and IgG3 were completely Tfh-dependent, while S-specific IgG2b and IgG2c were promoted by both Tfh and non-Tfh CD4$^+$ T cells (Fig. 1B). Consistent with their divergent requirement for Tfh cell help, S-specific IgG2c was induced earlier than S-specific IgG1 (Fig. S3A). S-specific IgM was unaffected by the absence of Tfh cells (Fig. S3B). Together, these results suggest that both Tfh cells and non-Tfh CD4$^+$ T cells promote the production of class-switched antibodies to SARS-CoV-2, though Tfh cells are specifically able to induce certain subclasses.

To corroborate these findings with a model that does not require AAV pre-transduction, we measured serum antibody titers of K18-hACE2 *Bcl6*$^{fl/fl}$ and *Bcl6*$^{fl/fl}$*Cd4*^{Cre} mice at 14 dpi with SARS-CoV-2 (Fig. 1C). K18-hACE2 *Bcl6*$^{fl/fl}$*Cd4*^{Cre} mice produced substantial levels of S-specific IgG antibodies, though reduced compared to K18-hACE2 *Bcl6*$^{fl/fl}$ mice (Fig. 1D). K18-hACE2 *Bcl6*$^{fl/fl}$*Cd4*^{Cre} mice also demonstrated similar patterns of IgG subclass production to AAV-hACE2 *Bcl6*$^{fl/fl}$*Cd4*^{Cre} mice. While S-specific IgG1 and IgG3 were completely abrogated in the absence of Tfh cells, S-specific IgG2b, IgG2c, and IgM were only partially reduced (Fig. 1D and S3C). This alternative model of SARS-CoV-2 infection therefore confirmed that certain IgG subclasses could be generated through Tfh-independent mechanisms.

Having observed Tfh-independent class-switched antibody production to SARS-CoV-2 infection, we asked whether this could also happen during non-live pathogen-driven immune stimulation such as vaccination. We hypothesized that

Downloaded from https://www.science.org at University of Massachusetts Worcester on January 12, 2022

while the strong and prolonged inflammatory response caused by infection might overcome the requirement for Tfh cell help, antibodies to vaccination would still be fully Tfh-dependent. We therefore vaccinated mice intramuscularly with a single dose of Moderna mRNA-1273 or Pfizer-BioNTech BNT162b2 mRNA vaccine and evaluated antibody responses at 14 days post vaccination (Fig. 1E). As with SARS-CoV-2 infection, mRNA vaccination induced both Tfh- and non-Tfh CD4$^+$ T cell-dependent S-specific IgG antibodies (Fig. 1F). mRNA vaccination promoted higher levels of S-specific IgG1 compared to infection, and some IgG1 could even be made in the absence of Tfh cells, contrasting with the complete Tfh cell dependence of infection-induced IgG1. S-specific IgG2b and IgG2c could similarly be made without Tfh cell help. S-specific IgG3 and IgM were minimally induced by mRNA vaccination (Fig. 1F and S3D). Therefore, class-switched antibodies to SARS-CoV-2 infection and vaccination are generated through both Tfh-dependent and -independent mechanisms.

Influenza virus infection induces Tfh-dependent and -independent antibodies

We next determined whether our findings with SARS-CoV-2 infection were generalizable to other models of respiratory viral infection. To this end, we infected mice with mouse-adapted influenza virus A/PR/8/34 H1N1 (PR8) and assessed antibody production at 14 dpi (Fig. 2A). Similar to SARS-CoV-2 infection, PR8 infection induced both Tfh-dependent and non-Tfh CD4$^+$ T cell-dependent IgG antibodies, while IgM was largely CD4$^+$ T cell-independent (Fig. 2, B and C). Again, PR8-specific IgG1 demonstrated a complete dependence on Tfh cell help, while PR8-specific IgG2b and IgG2c were promoted by both Tfh-dependent and -independent pathways (Fig. 2D). PR8-specific IgG3 was only partially dependent on Tfh and CD4$^+$ T cell help (Fig. 2D). Thus, both Tfh and non-Tfh CD4$^+$ T cells contribute to antibody production in two distinct models of respiratory viral infection.

Durable, high-affinity antibodies to SARS-CoV-2 can be made in the absence of Tfh cells

We then measured the affinity of the antibodies generated during SARS-CoV-2 and PR8 infection. As GCs are the conventional site of somatic hypermutation and affinity maturation (*2*), we expected that *Bcl6*$^{fl/fl}$ mice would generate high-affinity antibodies while *Bcl6*$^{fl/fl}$*Cd4*^{Cre} mice would generate low-affinity antibodies. Using the AAV-hACE2 model, we observed that *Bcl6*$^{fl/fl}$ mice produced high-affinity IgG antibodies to S as well as the spike receptor-binding domain (RBD) (Fig. 3A), a major target of neutralizing antibodies (*31*). In contrast, S- and RBD-specific IgG antibodies from *Ciita*$^{-/-}$ mice displayed minimal affinity compared to *Bcl6*$^{fl/fl}$ mice (25.7-fold reduction against S; 15.2-fold reduction against RBD). However, we discovered that antibodies from *Bcl6*$^{fl/fl}$*Cd4*^{Cre} mice still demonstrated substantial affinity toward S and RBD (2.7-fold and 1.9-fold reduction against S and RBD, respectively, relative to *Bcl6*$^{fl/fl}$ mice), suggesting that non-Tfh CD4$^+$ T cells could also promote high-affinity antibody production.

Similarly, K18-hACE2 *Bcl6*$^{fl/fl}$*Cd4*^{Cre} mice produced high-affinity antibodies to S and RBD (Fig. 3B), with a respective 2.6-fold and 1.7-fold reduction in affinity compared to controls. These data indicate that non-Tfh cells can support high-affinity antibody production in two separate models of SARS-CoV-2 infection. However, this was not the case with PR8 infection, as *Bcl6*$^{fl/fl}$*Cd4*^{Cre} mice produced IgG antibodies of minimal affinity to both PR8 and PR8 surface glycoprotein hemagglutinin (HA) (Fig. 3C). Therefore, the ability of non-Tfh cells to promote high-affinity antibodies may depend on the nature of the viral infection and the antigenic target.

We also evaluated the durability of S-specific IgG antibodies produced by K18-hACE2 *Bcl6*$^{fl/fl}$ and *Bcl6*$^{fl/fl}$*Cd4*^{Cre} mice following SARS-CoV-2 infection. Previous studies of viral infection have shown that antibody titers in Tfh-impaired mice are especially reduced at later timepoints (*10*, *11*, *17*). In SARS-CoV-2-infected K18-hACE2 *Bcl6*$^{fl/fl}$ mice, S-specific IgG levels peaked at 28 dpi and were stable through 84 dpi (Fig. 3, D and E). In K18-hACE2 *Bcl6*$^{fl/fl}$*Cd4*^{Cre} mice, S-specific IgG antibodies slowly declined after 28 dpi, but at 84 dpi still retained 50% of the antibody titer of 28 dpi (Fig. 3E and S4A). AAV-hACE2 *Bcl6*$^{fl/fl}$ and *Bcl6*$^{fl/fl}$*Cd4*^{Cre} mice displayed a similar pattern of antibody kinetics (Fig. S4, B and C).

Given that both *Bcl6*$^{fl/fl}$ and *Bcl6*$^{fl/fl}$*Cd4*^{Cre} mice demonstrated persistent S-specific IgG antibodies several months after infection, we investigated whether they had developed a virus-specific long-lived plasma cell compartment. We quantified S-specific IgG antibody-secreting cells (ASCs) in the bone marrow of K18-hACE2 *Bcl6*$^{fl/fl}$ and *Bcl6*$^{fl/fl}$*Cd4*^{Cre} mice at 85 dpi by ELISpot. S-specific IgG ASCs were detected in both groups of mice, though they were reduced tenfold in Tfh-deficient mice (Fig. 3F). However, Tfh-deficient mice also had fewer total bone marrow plasma cells (BMPCs), so the number of S-specific IgG ASCs per BMPC was similar between *Bcl6*$^{fl/fl}$ and *Bcl6*$^{fl/fl}$*Cd4*^{Cre} mice (Fig. 3, F and G). Taken together, these results indicate that Tfh-independent antibodies to SARS-CoV-2 can still be high-affinity and durable – two important qualities usually attributed to Tfh-dependent responses.

Tfh-deficient mice demonstrate similar V gene usage but impaired mutation selection compared to Tfh-sufficient mice

To ascertain how Tfh-deficient mice generate high-affinity antibodies to S and RBD, we considered two non-mutually exclusive hypotheses: 1) unmutated, germline-encoded B cell receptors (BCRs) in the murine V(D)J repertoire may already possess high affinity for S and/or RBD, and 2) S-specific B cells may undergo somatic hypermutation (SHM) even in the

Downloaded from https://www.science.org at University of Massachusetts Worcester on January 12, 2022

absence of Tfh cells and GCs. The former possibility has already been observed for patient-derived SARS-CoV-2-specific antibodies, which demonstrate high potency with minimal SHM (*32*–*36*). The latter possibility is supported by prior reports of SHM occurring at extrafollicular sites during chronic autoimmunity and bacterial infection (*37*–*39*).

To investigate these two possibilities, we isolated S-specific plasmablasts from K18-hACE2 *Bcl6*$^{fl/fl}$ and *Bcl6*$^{fl/fl}$*Cd4*^{Cre} mice at 14 dpi and performed BCR sequencing (Fig. S5, A to B). After read preprocessing and V(D)J gene annotation, we clustered the resulting BCR sequences into clonal families, identifying a range of 131 to 694 distinct clones in each sample (Fig. 4A and S5C). We assessed the relative proportions of the 10 largest clones in each sample, finding that the top-ranked clone in each sample comprised 8% to 56% of total BCR sequences recovered, while the top 10 clones accounted for 40% to 76% of total BCR sequences (Fig. 4A). These findings indicate that clonal expansion had occurred in both *Bcl6*$^{fl/fl}$ and *Bcl6*$^{fl/fl}$*Cd4*^{Cre} mice. To further characterize the clonal architecture of the BCR repertoires, we calculated the diversity of each BCR repertoire using the Shannon entropy score and Simpson's diversity index. The diversity of BCR repertoires in *Bcl6*$^{fl/fl}$ and *Bcl6*$^{fl/fl}$*Cd4*^{Cre} mice was not statistically different by either metric, though we noted a trend toward increased diversity in the *Bcl6*$^{fl/fl}$*Cd4*^{Cre} mice (Fig. 4B).

Analysis of immunoglobulin heavy-chain variable (V) gene usage frequencies revealed that out of all candidate V genes, 22 were utilized at ≥ 2% frequency in ≥ 2 samples. Usage of most V genes was not significantly different between *Bcl6*$^{fl/fl}$ and *Bcl6*$^{fl/fl}$*Cd4*^{Cre} mice (Fig. 4C). However, we observed that *Ighv1-72*, *Ighv11-2*, and *Ighv5-6* were used more frequently in BCRs from *Bcl6*$^{fl/fl}$*Cd4*^{Cre} mice compared to *Bcl6*$^{fl/fl}$ mice. Examining the median usage frequencies, *Ighv1-26* was the most frequently used V gene in *Bcl6*$^{fl/fl}$ mice, while BCRs from *Bcl6*$^{fl/fl}$*Cd4*^{Cre} mice most frequently used *Ighv1-72*. Repeating this analysis on the clone-level, rather than the individual BCR sequence-level, similarly revealed that usage of most V genes was not significantly different in the absence of Tfh cells (Fig. S5D). Thus, while Tfh-deficient mice did not exhibit overt changes in V gene usage, there were nevertheless differences that could reflect the distinct nature of the T cell help in these mice.

COVID-19 patient studies have identified potent RBD-specific antibodies with recurrent V gene usage and minimal SHM (*32*–*36*). To explore whether there are murine V genes that can similarly contribute to high-affinity S- or RBD-specific antibodies, we identified the murine V genes expressed in our dataset (≥ 2% frequency in ≥ 2 samples) with the greatest homology to frequently used and minimally mutated human V genes (Fig. 4D and S5, E and F) (*32*–*36*). Human IGHV3-53 and IGHV3-30 demonstrated the highest homology to murine *Ighv5-6* and *Ighv11*-2, which were utilized more frequently in BCRs from *Bcl6*$^{fl/fl}$*Cd4*^{Cre} compared to *Bcl6*$^{fl/fl}$ mice (Fig. 4C). Murine V genes most similar to human IGHV1-58, IGHV3-30-3, and IGHV1-69 were used at comparable frequencies between BCRs from *Bcl6*$^{fl/fl}$ and *Bcl6*$^{fl/fl}$*Cd4*^{Cre} mice. Taken together, these data suggest that homologous human and murine V genes may contribute to potent SARS-CoV-2-specific antibodies. Furthermore, preferential usage of these V genes in Tfh-deficient mice may enable the production of high-affinity antibodies with minimal SHM.

To investigate whether SHM could still occur in Tfh-deficient mice, we determined the mutational profiles of each clonal consensus sequence compared to the mouse germline. We found evidence of SHM in S-specific IgG plasmablasts from *Bcl6*$^{fl/fl}$*Cd4*^{Cre} mice, albeit at significantly lower frequency compared to plasmablasts from *Bcl6*$^{fl/fl}$ mice (Fig. 4E). Overall, 66.28% ± 6.36% (mean ± s.e.m.) of clones from *Bcl6*$^{fl/fl}$ mice had somatic mutations, compared to 41.61% ± 3.88% of clones from *Bcl6*$^{fl/fl}$*Cd4*^{Cre} mice (Fig. 4F). This contrast was especially pronounced when considering the percentage of clones with two or more somatic mutations: 46.04% ± 6.13% of *Bcl6*$^{fl/fl}$ clones and 14.81% ± 1.25% of *Bcl6*$^{fl/fl}$*Cd4*^{Cre} clones (Fig. 4F). Similar results were obtained by comparing individual BCR sequences (Fig. S5G).

We further compared mutation selection strength in *Bcl6*$^{fl/fl}$ and *Bcl6*$^{fl/fl}$*Cd4*^{Cre} BCR repertoires using BASELINe, which determines the ratio of non-synonymous to synonymous mutations compared to a reference model (*40*, *41*). Validating the BASELINe analytical approach, selection strength was positive in the complementarity determining regions (CDRs) of BCRs from *Bcl6*$^{fl/fl}$ mice and negative in the framework regions (FWRs) (Fig. 4G). This is consistent with the fact that CDRs are the main determinants of antigen specificity and thus enriched in non-synonymous mutations, while FWRs generally serve as structural scaffolds, making them less tolerant of residue-altering mutations. Across both CDRs and FWRs, we found that the ratio of non-synonymous to synonymous mutations was significantly lower in S-specific IgG plasmablasts from *Bcl6*$^{fl/fl}$*Cd4*^{Cre} mice compared to *Bcl6*$^{fl/fl}$ mice (Fig. 4G), indicating that Tfh cells are required for positive selection of mutated B cell clones against SARS-CoV-2. Collectively, our analysis of the BCR repertoire after SARS-CoV-2 infection suggests that both V gene usage patterns and low levels of SHM, though without mutation selection, may contribute to the production of high-affinity Tfh-independent antibodies.

Tfh cells focus the antibody repertoire but are dispensable for broad coverage of SARS-CoV-2 epitopes

We next characterized the antibody epitope repertoire of Tfh-dependent versus -independent responses to SARS-CoV-2. Sera from AAV-hACE2 *Bcl6*$^{fl/fl}$ and *Bcl6*$^{fl/fl}$*Cd4*^{Cre} mice at 14 dpi were profiled using a bacterial display library of 2410

Downloaded from https://www.science.org at University of Massachusetts Worcester on January 12, 2022

linear peptides tiling the entire SARS-CoV-2 proteome (Fig. 5A, Data file S1). We first compared the diversity of antibody epitope reactivity, calculating the Shannon entropy, Simpson's diversity index, and the repertoire focusing index within each sample. We observed that antibody diversity assessed by Shannon entropy and Simpson's diversity index was significantly decreased in *Bcl6*$^{fl/fl}$ mice compared to *Bcl6*$^{fl/fl}$*Cd4*^{Cre} mice, while the degree of repertoire focusing was increased (Fig. 5B, Data file S2). These findings were robust to variations in read counts (Fig. S6A). These results suggest that Tfh cells help focus the antibody response to particular SARS-CoV-2 epitopes while non-Tfh cells promote antibodies to a wider array of targets.

Given these changes in antibody diversity, we next explored whether there were differences in antibody reactivity at the level of individual linear epitopes. After normalizing for read count variations using the median of ratios method (Fig. S6B), we identified epitopes that were comparatively enriched or depleted in *Bcl6*$^{fl/fl}$ versus *Bcl6*$^{fl/fl}$*Cd4*^{Cre} mice (Fig. 5C). We found that seven epitopes were enriched in *Bcl6*$^{fl/fl}$ mice, while one epitope was depleted (Fig. 5D). Five of the seven enriched epitopes were derived from S: aa661-672 (proximal to S1/S2 cleavage site), aa801-812 (fusion peptide [FP] 1), aa817-828 (FP2), aa977-988 (heptad repeat [HR] 1), and aa1145-1156 (between HR1/HR2). On the other hand, aa145-156 (N-terminal domain) from S was comparatively depleted in *Bcl6*$^{fl/fl}$ mice.

To further investigate alterations in epitope reactivity, we converted the normalized counts to z-scores on a sample-by-sample basis, such that the z-scores would denote the relative rank of a specific epitope within a particular sample (Fig. S6C). Consistent with our prior analyses, the average z-scores in *Bcl6*$^{fl/fl}$ versus *Bcl6*$^{fl/fl}$*Cd4*^{Cre} mice were similar across most SARS-CoV-2 proteins, with the exception of regions within the S and ORF3a proteins (Fig. 5E). In particular, the regression lines for non-S proteins all closely followed the line of identity, indicating that the relative ranks of epitopes from non-S proteins were largely similar in the presence or absence of Tfh cells. These analyses therefore indicate that, while Tfh cells are dispensable for antibody production against most SARS-CoV-2 epitopes, they are required to focus the antibody response against certain S-derived epitopes.

RBD-specific antibodies are generated in the absence of Tfh cells

Analyzing antibody epitope reactivity along the length of S, we observed that the majority of epitopes enriched in *Bcl6*$^{fl/fl}$ mice (17/21 epitopes with differential average z-score > 1) were found in the S2 domain (aa686-1273; Fisher's exact test $p = 0.0012$) (Fig. 6A), which mediates fusion of viral and target cell membranes (*42*). These included most of the aforementioned S-derived epitopes that were significantly enriched (Fig. 5C), as well as contiguous epitopes whose enrichment did not reach statistical significance in the epitope-level analysis. For example, several epitopes in the fusion peptide were enriched adjacent to the significantly enriched epitopes aa801-812 and aa817-828 (Fig. S6D). Many of these epitopes are highly conserved across human coronaviruses (hCoVs) as well as the emerging variants of concern (Fig. 6A). Interestingly, the enriched epitopes spanning FP1/FP2 and preceding HR2 have also been identified in numerous studies profiling the antibody epitope repertoire of COVID-19 patients (*43*, *44*). Given their immunodominance and conservation across hCoVs, these epitopes have been proposed as targets for a pan-coronavirus vaccine.

In contrast, *Bcl6*$^{fl/fl}$ and *Bcl6*$^{fl/fl}$*Cd4*^{Cre} mice demonstrated similar antibody reactivity to most epitopes within the RBD (Fig. 6B), the target of most neutralizing antibodies (*31*). However, as most antibodies to RBD likely recognize conformational epitopes (*43*, *44*), we also measured RBD-specific antibodies by ELISA using full-length RBD. RBD-specific IgG titers normalized by total S-specific IgG were similar between *Bcl6*$^{fl/fl}$ and *Bcl6*$^{fl/fl}$*Cd4*^{Cre} mice (Fig. 6C). Thus, while Tfh cells focus the antibody response against immunodominant S2 epitopes, non-Tfh cells still promote antibodies against the primary target of neutralization, RBD.

Tfh-dependent and -independent antibodies demonstrate similar neutralization potency against homologous SARS-CoV-2 as well as the B.1.351 variant of concern

We next evaluated the function of antibodies from *Bcl6*$^{fl/fl}$ and *Bcl6*$^{fl/fl}$*Cd4*^{Cre} mice following SARS-CoV-2 infection. While we had observed that Tfh-independent antibody responses to the virus lacked IgG1/IgG3 subclasses (Fig. 1, B and D) and S2 epitope focusing (Fig. 6A), these antibodies were still high-affinity (Fig. 3, A and B) and could target the RBD (Fig. 6C). We therefore predicted that Tfh-independent antibodies would demonstrate similar neutralizing function against homologous SARS-CoV-2 (USA-WA1/2020) as those generated with Tfh cell help. Using vesicular stomatitis virus (VSV) pseudotyped with USA-WA1/2020 S protein, we measured the neutralization titer (the reciprocal serum dilution achieving 50% neutralization of pseudovirus infection, NT50) of sera from AAV-hACE2 *Bcl6*$^{fl/fl}$ and *Bcl6*$^{fl/fl}$*Cd4*^{Cre} mice. *Bcl6*$^{fl/fl}$ sera exhibited increased NT50 (Fig. 7A), which was expected given their higher levels of S-specific IgG antibodies (Fig. 1B). However, by normalizing NT50 to S-specific IgG levels in each sample, we observed that the neutralization potency indices of *Bcl6*$^{fl/fl}$ and *Bcl6*$^{fl/fl}$*Cd4*^{Cre} sera were similar and actually trended higher for *Bcl6*$^{fl/fl}$*Cd4*^{Cre} sera (Fig. 7A).

We next tested the same sera against VSV pseudotyped with S protein from the B.1.351 variant of concern. Multiple studies have shown that B.1.351 S mutations, particularly those in the RBD, disrupt binding by neutralizing antibodies and facilitate immune escape (*45*, *46*). We therefore

Downloaded from https://www.science.org at University of Massachusetts Worcester on January 12, 2022

hypothesized that increased focusing of Tfh-dependent antibodies against conserved S2 epitopes would enable *Bcl6*$^{fl/fl}$ sera to better neutralize B.1.351 pseudovirus than *Bcl6*$^{fl/fl}$*Cd4*^{Cre} sera. While *Bcl6*$^{fl/fl}$ sera exhibited greater NT50 than *Bcl6*$^{fl/fl}$*Cd4*^{Cre} sera, we found that the neutralization potency index of *Bcl6*$^{fl/fl}$*Cd4*^{Cre} sera again trended higher than that of *Bcl6*$^{fl/fl}$ sera (Fig. 7B). Nevertheless, both *Bcl6*$^{fl/fl}$ and *Bcl6*$^{fl/fl}$*Cd4*^{Cre} sera demonstrated an approximately 10-fold reduction in NT50 against the B.1.351 variant compared to USA-WA1/2020 (Fig. 7C), consistent with previous studies (*45*, *46*). Our findings therefore indicate that Tfh-independent antibodies exhibit similar, if not increased, neutralization potency to Tfh-dependent antibodies in vitro and that S2 epitope focusing does not improve neutralization activity against the B.1.351 variant of concern.

Finally, we assessed the function of *Bcl6*$^{fl/fl}$ and *Bcl6*$^{fl/fl}$*Cd4*^{Cre} sera against SARS-CoV-2 in vivo. To this end, we transferred sera from AAV-hACE2 *Bcl6*$^{fl/fl}$ or *Bcl6*$^{fl/fl}$*Cd4*^{Cre} mice infected with SARS-CoV-2 (USA-WA1/2020) into naïve K18-hACE2 mice (Fig. 7D). *Bcl6*$^{fl/fl}$ sera was given undiluted or diluted 7- to 9-fold to match the S-specific IgG titer of *Bcl6*$^{fl/fl}$*Cd4*^{Cre} sera in a given experiment. One day later, we infected the K18-hACE2 recipients with homologous SARS-CoV-2 and then measured viral burden in the lungs at 4 dpi. Undiluted *Bcl6*$^{fl/fl}$ sera led to the greatest reduction in viral burden (Fig. 7, E and F), indicating that, as expected, antibody titer is an important determinant of protection against viral challenge. However, once matched for S-specific IgG titer, *Bcl6*$^{fl/fl}$ and *Bcl6*$^{fl/fl}$*Cd4*^{Cre} sera provided a similar degree of protection (Fig. 7, E and F), corroborating our in vitro findings that Tfh-dependent and -independent antibodies exhibit similar neutralization potency. Taken together, these results demonstrate that Tfh-independent antibodies efficiently neutralize both homologous SARS-CoV-2 and the B.1.351 variant of concern but that optimal protection in vivo still relies on Tfh cells to generate high antibody titers.

DISCUSSION

While protective antibodies are generally thought to originate from Tfh/GC-dependent pathways, it is unclear what happens to the antibody response when these structures are disrupted, as has been observed in patients with severe SARS-CoV-2 infection (*6*, *7*). We found that certain class-switched antibodies were reduced but still present in Tfh-deficient mice following SARS-CoV-2 or influenza A virus infection, as well as SARS-CoV-2 vaccination. Though BCR analysis demonstrated impairment of SHM and mutation selection, Tfh-independent antibodies to SARS-CoV-2 were still high-affinity. They were also durable and demonstrated more diverse epitope reactivity compared to Tfh-dependent antibodies. Importantly, Tfh-independent antibody responses neutralized both homologous SARS-CoV-2 (USA-WA1/2020) and the B.1.351 variant of concern and were functional in vitro and in vivo (Fig. S7).

Our findings raise the question of which CD4$^+$ T cell subset promotes protective class-switched antibodies in the absence of Tfh cells. It has previously been shown in the setting of influenza vaccination that Th1 cells make IFN-γ along with IL-21 to induce IgG2c antibodies (*19*). Though less mutated and of lower avidity, these Th1-driven antibodies still neutralize influenza virus in vitro and protect from lethal challenge in vivo (*19*). Additionally, a recent study proposed a division of labor between Th1 cells and Tfh cells in promoting IgG2c class switching and supporting GC growth, respectively, during influenza virus infection (*47*). Therefore, it is possible that lymph node-resident Th1 cells are also responsible for the IgG2c antibodies we observed to SARS-CoV-2 infection and vaccination (*48*). Contrary to the consistent Tfh-independent induction of IgG2c, IgG1 demonstrated a divergent requirement for Tfh cell help between SARS-CoV-2 infection and vaccination. These findings align with prior literature (*17*, *20*, *23*), suggesting that there may be different cellular requirements for IgG1 in the setting of diverse immune stimuli. Similarly, CD4$^+$ T cells are dispensable for IgG3 in response to influenza virus infection (*49*), but we observed that IgG3 to SARS-CoV-2 was completely dependent on Tfh cell help. Thus, the same subclass may be produced by disparate mechanisms even during different viral infections. Finally, it is important to consider whether incomplete deletion of Tfh cells could contribute to antibody responses in *Bcl6*$^{fl/fl}$*Cd4*^{Cre} mice. This same mouse model demonstrates complete abrogation of IgE and IgG1 to allergens (*26*), and our characterization of cells and structures in the medLN support a lack of T cell-infiltrated, organized GCs in *Bcl6*$^{fl/fl}$*Cd4*^{Cre} mice; therefore, we conclude that highly specific and long-lived antibodies can be produced through Tfh-independent mechanisms likely dependent on the nature of infection or vaccination.

A surprising finding from our work was that SARS-CoV-2, but not influenza A virus, induced high-affinity Tfh-independent antibodies. As a possible mechanism for this finding, S-specific BCRs from Tfh-deficient mice used V genes highly homologous to human V genes that generate potent S-specific antibodies with minimal SHM (*32*–*36*). Furthermore, S-specific BCRs still experienced low levels of SHM in the absence of Tfh cell help. Though SHM conventionally occurs in GCs (*2*), it has also been shown to occur at extrafollicular sites during bacterial infection and chronic autoimmunity (*37*–*39*). However, in the absence of Tfh cell help, mutated B cell clones did not experience positive selection, differentiating this process from classical affinity maturation. In this non-canonical pathway of high-affinity antibody production, non-Tfh CD4$^+$ T cells may help by selecting naïve B cells that already express potent S-specific BCRs as well as supporting plasmablast differentiation of lowly mutated B cell clones. Our findings also suggest that long-lived plasma cells can

Downloaded from https://www.science.org at University of Massachusetts Worcester on January 12, 2022

emerge from this pathway, providing a durable source of humoral immunity.

Epitope profiling revealed that Tfh cells focus the antibody repertoire against S2-derived epitopes that are highly conserved across human coronaviruses as well as the emerging variants of concern. These same epitopes have been repeatedly identified in studies profiling the antibody repertoire of COVID-19 patients (*43*, *44*), suggesting that the immunodominance of these epitopes in humans is mediated by Tfh cells. It has also been proposed that S2-reactive antibodies in people are primed by prior infections with endemic human coronaviruses (*43*). Given our findings in mice, which were not exposed to other coronaviruses prior to SARS-CoV-2 infection, it is likely that the intrinsic qualities of these S2-derived epitopes also contribute to their immunodominance. In addition, broadly neutralizing betacoronavirus antibodies with S2 specificity have recently been described, suggesting the use of S2-derived epitopes as targets for a pan-coronavirus vaccine (*50*). However, S2-specific antibodies are generally less potent neutralizers than RBD-specific antibodies and may even demonstrate little neutralization in vitro despite providing protection in vivo (*50*, *51*). This provides a possible explanation for why we observed slightly lower neutralization potency indices of Tfh-dependent antibodies enriched for S2 epitope reactivity compared to more diverse Tfh-independent antibodies. Alternatively, the less focused antibody repertoire of Tfh-deficient mice may better neutralize SARS-CoV-2 by targeting multiple sites of vulnerability, similar to previous findings of GC inhibition promoting a broader antibody response and enhanced heterosubtypic immunity to influenza virus infection (*52*).

While long-lived, high-affinity, neutralizing antibody responses conventionally depend on Tfh cells, we found that antibodies of similar quality, though not quantity, could be generated with the help of non-Tfh $CD4^+$ T cells. Therefore, multiple pathways involving different $CD4^+$ T cell subsets likely exist to promote protective antiviral humoral immunity (*48*). Tfh-independent responses may serve as a parallel mechanism for producing protective antibodies in settings of Tfh/GC impairment, such as COVID-19-induced inflammation and advanced age (*6*, *53*). Understanding this additional axis of antiviral antibody production may therefore inform more effective vaccine design and help broaden our understanding of how T cell-dependent humoral immunity is generated.

MATERIALS AND METHODS

Study design

The purpose of this study was to define the Tfh-independent antibody response to respiratory viruses, including SARS-CoV-2 and influenza A virus, and SARS-CoV-2 mRNA vaccination. Experiments included intranasal infection or intramuscular vaccination. Analyses included serum antibody profiling, BCR sequencing, T cell and B cell phenotyping from mediastinal lymph nodes and bone marrow, and lung viral burden. $Bcl6^{fl/fl}$ and $Bcl6^{fl/fl}Cd4^{Cre}$ littermates were used for all experiments. For serum transfer experiments, K18-hACE2 recipients were randomized to age- and sex-matched groups for different treatments. The investigators were not blinded, with the exception of ELISpot counting. The number of experimental replicates is indicated in the figure legends.

Mice

$Bcl6^{fl/fl}$ [B6.129S(FVB)-$Bcl6^{tm1.1Dent}$/J (*22*)], $Cd4^{Cre}$ [B6.Cg-Tg(Cd4-cre)1Cwi/BfluJ (*54*)], $Ciita^{-/-}$ [B6.129S2-$Ciita^{tm1Ccum}$/J (*27*)], and K18-hACE2 [B6.Cg-Tg(K18-ACE2)2Prlmn/J (*30*)] mice were purchased from Jackson Laboratory. $Bcl6^{fl/fl}$ mice were crossed with $Cd4^{Cre}$ mice to generate $Bcl6^{fl/fl}Cd4^{Cre}$ mice. K18-hACE2 mice were crossed with $Bcl6^{fl/fl}Cd4^{Cre}$ mice to generate K18-hACE2 $Bcl6^{fl/fl}$ and $Bcl6^{fl/fl}Cd4^{Cre}$ mice. Mice were bred in-house using mating trios to enable utilization of littermates for experiments. Mice of both sexes between 6 and 10 weeks old were used for this study. Animal use and care was approved in agreement with the Yale Animal Resource Center and Institutional Animal Care and Use Committee according to the standards set by the Animal Welfare Act.

Cell lines

Huh7.5 (CVCL-7927), Vero-E6 (CRL-1586), and 293T (CRL-3216) cells were from ATCC. Cell lines were cultured in Dulbecco's Modified Eagle Medium (DMEM) with 10% heat-inactivated fetal bovine serum (FBS) and 1% Penicillin/Streptomycin. All cell lines tested negative for *Mycoplasma* spp.

AAV-hACE2 transduction

Adeno-associated virus 9 expressing hACE2 from a CMV promoter (AAV-hACE2) was purchased from Vector Biolabs (SKU AAV-200183). Mice were anesthetized by intraperitoneal injection of ketamine (50 mg/kg) and xylazine (5 mg/kg). The rostral neck was shaved and disinfected with povidone-iodine. After a 5-mm incision was made, the salivary glands were retracted and the trachea visualized. Using a 31G insulin syringe, 10^{11} genomic copies of AAV-hACE2 in 50 μl PBS were injected into the trachea. The incision was closed with 3M Vetbond tissue adhesive, and mice were monitored until full recovery.

Viruses

SARS-CoV-2 P1 stock was generated by inoculating Huh7.5 cells with SARS-CoV-2 isolate USA-WA1/2020 (BEI Resources, NR-52281) at a MOI of 0.01 for three days. The P1 stock was then used to inoculate Vero-E6 cells, and the supernatant was harvested after three days at 50% cytopathic effect. The supernatant was clarified by centrifugation (450 × *g* for 5 min), filtered through a 0.45-micron filter, and stored in aliquots at -80°C. For infection of AAV-hACE2 mice, virus was concentrated by mixing one volume of cold 4X PEG-it Virus Precipitation Solution (40% wt/vol PEG-8000 and 1.2

Downloaded from https://www.science.org at University of Massachusetts Worcester on January 12, 2022

M NaCl) with three volumes of viral supernatant. The mixture was incubated overnight at 4°C and then centrifuged at 1500 × *g* for 60 min at 4°C. The pelleted virus was resuspended in PBS and stored in aliquots at -80°C. Virus titer was determined by plaque assay using Vero-E6 cells (*55*).

Influenza virus A/PR/8/34 H1N1 (PR8) expressing the ovalbumin OT-II peptide was grown for 2.5 days at 37°C in the allantoic cavities of 10-day-old specific-pathogen-free fertilized chicken eggs. Harvested virus was centrifuged at 3000 × *g* for 20 min at 4°C to remove debris and stored in aliquots at -80°C. Virus titer was determined by plaque assay on Madin-Darby canine kidney cells (*56*).

For all infections, mice were anesthetized using 30% vol/vol isoflurane diluted in propylene glycol (30% isoflurane) and administered SARS-CoV-2 or PR8 intranasally in 50 μl PBS. AAV-hACE2 *Bcl6*$^{fl/fl}$, *Bcl6*$^{fl/fl}$*Cd4*^{Cre}, and *Ciita*$^{-/-}$ mice were infected with 1.2×10^6 PFU of SARS-CoV-2. K18-hACE2 *Bcl6*$^{fl/fl}$ and *Bcl6*$^{fl/fl}$*Cd4*^{Cre} mice were infected with 20 PFU of SARS-CoV-2. K18-hACE2 mice in serum transfer experiments were infected with 100 PFU of SARS-CoV-2. *Bcl6*$^{fl/fl}$, *Bcl6*$^{fl/fl}$*Cd4*^{Cre}, and *Ciita*$^{-/-}$ mice were infected with 70 PFU of PR8. All work with SARS-CoV-2 was performed in a biosafety level 3 (BSL3) facility with approval from the office of Environmental Health and Safety and the Institutional Animal Care and Use Committee at Yale University.

mRNA vaccination

Used vials of Moderna mRNA-1273 and Pfizer-BioNTech BNT162b2 mRNA vaccine were obtained from Yale Health within 6 hours of opening. All vials contained less than one full dose per vial, and no vaccines were diverted for the purpose of this study. Mice were anesthetized using 30% isoflurane and administered 1 μg of either Moderna or Pfizer-BioNTech vaccine intramuscularly in 50 μl PBS. Vaccine was injected into the right hamstring muscles with a 31G insulin syringe.

Enzyme-linked immunosorbent assay (ELISA)

Sera were incubated with a final concentration of 0.5% Triton X-100 and 0.5 mg/ml RNase A for 30 min at room temperature to inactivate potential SARS-CoV-2. SARS-CoV-2 stabilized spike glycoprotein (BEI Resources, NR-53257) (*57*), SARS-CoV-2 spike glycoprotein receptor-binding domain (RBD) (BEI Resources, NR-52946), and influenza virus A/PR/8/34 H1N1 hemagglutinin (HA) protein (Sino Biological, 11684-V08H) were coated at a concentration of 2 μg/ml in carbonate buffer on 96-well MaxiSorp plates (Thermo Fisher) overnight at 4°C. PR8 was inactivated with 1% Triton X-100 for 1 hour at 37°C and coated at a concentration of 20 μg/ml in carbonate buffer. Plates were blocked with 1% BSA in PBS for 1 hour at room temperature. Serum samples were serially diluted in 1% BSA in PBS and incubated in plates for 2 hours at room temperature. Antibody isotypes were detected with anti-mouse IgG-HRP (1013-05), anti-mouse IgG1-HRP (1073-05), anti-mouse IgG2b-HRP (1093-05), anti-mouse IgG2c-HRP (1077-05), or anti-mouse IgG3-HRP (1103-05) from Southern Biotech or anti-mouse IgM-HRP (550588) from BD Biosciences by incubating for 1 hour at room temperature. Plates were developed with TMB Stabilized Chromogen (Thermo Fisher), stopped with 3 N hydrochloric acid, and read at 450 nm on a microplate reader. Background was determined as twice the average OD value of blank wells. Pooled sera from mice infected with SARS-CoV-2 or PR8 were used as reference standards to calculate arbitrary units. To measure antibody affinity, serial dilutions of serum samples were plated in duplicate. After incubation of serum samples, a 10-min wash with 5.3 M urea was performed on one set of the samples. Percentage of IgG binding after urea wash was calculated by dividing the area under the curve for each sample with urea wash by that without urea wash.

Enzyme-linked immunosorbent spot (ELISpot)

SARS-CoV-2 stabilized spike glycoprotein (BEI Resources, NR-53257) (*57*) was coated at a concentration of 2 μg/ml in carbonate buffer on 96-well MultiScreen HTS IP Filter plates (Millipore) overnight at 4°C. Plates were blocked with complete RPMI (10% heat-inactivated FBS, 1% Penicillin/Streptomycin, 2 mM L-glutamine, 1 mM sodium pyruvate, 10 mM HEPES, 55 μM 2-mercaptoethanol) for 4 hours at 37°C. Bone marrow cells were isolated from the left femur + tibia of mice infected with SARS-CoV-2. Red blood cells were lysed with RBC Lysis Buffer (BioLegend) for 2 min. Cells were resuspended in complete RPMI and plated in duplicate at three dilutions (1/5, 1/10, and 1/20 of total bone marrow cells) for 20 hours at 37°C. Plates were washed six times with PBS-T (0.01% Tween-20), followed by incubation with anti-mouse IgG-Alkaline Phosphatase (Southern Biotech, 1030-04) in PBS with 0.5% BSA for 2 hours at room temperature. Plates were then washed three times with PBS-T and three times with PBS. Spots were developed with Vector® Blue Substrate Kit (Vector Laboratories, SK-5300) and imaged with an ImmunoSpot analyzer (Cellular Technology Limited). Spots were counted manually by a blinded investigator.

Flow cytometry and cell sorting

Mediastinal lymph nodes (medLN) were homogenized with a syringe plunger and filtered through a 70-μm cell strainer. Red blood cells were lysed with RBC Lysis Buffer (BioLegend) for 1 min. Single-cell preparations were resuspended in PBS with 2% FBS and 1 mM EDTA and pre-incubated with Fc block (2.4G2; BD Biosciences, 553141) for 5 min at room temperature before staining. Cells were stained with the following antibodies or viability dye for 30 min at 4°C: anti-CD4 (RM4-5; BioLegend, 100568), TCRβ (H57-597; BioLegend, 109228), PD-1 (RMP1-30; BioLegend, 109110), CD44 (IM7; BioLegend, 103047), PSGL-1 (2PH1; BD Biosciences, 563448), Ly6C (HK1.4; BioLegend, 128005), B220 (RA3-6B2; BioLegend, 103260), Fas (Jo2; BD Biosciences, 563647), GL7

Downloaded from https://www.science.org at University of Massachusetts Worcester on January 12, 2022

(GL7; BioLegend, 144610), CD138 (281-2; BioLegend, 142514), and LIVE/DEAD Fixable Aqua (Thermo Fisher, L34966). CXCR5 (L138D7; BioLegend, 145510) was stained for 25 min at room temperature. Samples for flow cytometry were fixed with 4% paraformaldehyde for 30 min at room temperature before removal from BSL3 facility. Samples were acquired on a CytoFLEX S (Beckman Coulter) and analyzed using FlowJo software (BD).

For cell sorting, medLN were stained with aforementioned B cell surface markers and viability dye, along with 2 μg/ml FLAG-tagged SARS-CoV-2 spike protein (GenScript, Z03481) for 30 min at 4°C (*58*). Cells were then stained with both APC- and PE-conjugated anti-FLAG antibodies (BioLegend, 637309 and 637307) to double-stain spike-specific B cells. Spike-specific plasmablasts (live $CD138^{hi}Spike^{+}$) were sorted into 350 μl Buffer RLT Plus (Qiagen) with 1% β-mercaptoethanol. RLT lysate was vortexed for 1 min, frozen on dry ice, and then stored at -80°C. Cell sorting was performed on a FACSAria II (BD Biosciences) in the BSL3 facility.

BCR library preparation

RNA from spike-specific B cells was isolated using the RNeasy Plus Micro Kit (Qiagen) following manufacturer's instructions. BCR libraries were prepared using the NEBNext® Single Cell/Low Input cDNA Synthesis & Amplification Module (NEB, E6421) and NEBNext® Immune Sequencing Kit (NEB, E6330), with additional reagents provided by NEB to integrate the two kits. 1-20 ng of high-quality RNA with RIN score ≥ 8 was used as input. Libraries were analyzed by Bioanalyzer High Sensitivity DNA assay, pooled in equal amounts with PhiX spike-in, and sequenced on an Illumina MiSeq using the V3 kit, with 325 bp for read 1 and 275 bp for read 2.

BCR repertoire analysis

UMI-barcoded paired-end sequencing reads were processed and analyzed with the Immcantation suite (Docker image v4.3.0). Read preprocessing was performed with the presto-abseq pipeline interface for pRESTO (v0.7.0) (*59*) with default settings, using mouse constant region primers, isotype-specific internal constant region sequences, and template switch sequences provided by NEB. The preprocessed reads were aligned to the mouse germline V(D)J genes with the changeo-igblast pipeline interface for Change-O (v1.2.0) (*60*) and IgBLAST (v1.17.1). Productive sequences aligning to immunoglobulin heavy chains were retained for further analysis. Each sequence was annotated with the corresponding germline V(D)J sequence, masking N/P and D-segment regions. Spectral clustering was performed using SCOPer (v1.2.0) (*61*) to identify clonally-related sequences, based on the level of junction region homology and the mutation profiles in the V-J segments. Following clonal clustering, consensus germline sequences for each clone were reconstructed as above.

Sequences aligning to constant regions other than IgM, IgA, or IgG were filtered out from further analysis. Relative clonal proportions were calculated by tabulating the number of UMI-barcoded sequences belonging to each clonal family. Clonal proportions were visualized as pie charts, with the top 10 clones each represented individually and all other clones combined into one category. Given the wide variation in the number of clones across samples, in order to characterize the diversity of each BCR repertoire, 100 clones were randomly sampled from each repertoire to calculate Shannon entropy and Simpson's diversity index. This process was repeated 100 times for each sample, ultimately taking the average value across all repeats.

Downstream analysis was performed using Alakazam (v1.2.0) and SHazaM (v1.1.0) (*40*, *41*). Heavy chain V gene usage frequencies were calculated on either the sequence-level or the clone-level. For the sequence-level analysis, the frequency of individual UMI-barcoded BCR sequences aligned to each V gene was calculated. For the clone-level analysis, the frequency of clones aligned to each V gene was determined, taking the consensus V gene assignment across all constituent UMI-barcoded sequences belonging to each clone. V genes that were present at ≥ 0.02 frequency in ≥ 2 repertoires were retained for visualization purposes. The most frequently used human V genes in SARS-CoV-2 specific antibodies from patients were determined by mining the CoV-AbDab database (*62*). Out of the mouse V genes that were expressed at ≥ 0.02 clone-level frequency in ≥ 2 repertoires, those that are most similar to the top-ranked human V genes were identified with BLAST. For visualization, alignment of mouse and human V genes was performed using Clustal Omega and visualized using Jalview with the Clustal X color scheme. Lineage trees were constructed with dowser (*63*), building the maximum parsimony tree for all constituent BCRs in a clone. Branch lengths were scaled by the number of mutations between nodes. To facilitate qualitative comparisons, the pair of $Bcl6^{fl/fl}$ and $Bcl6^{fl/fl}Cd4^{Cre}$ mice with the greatest similarity in the total number of clones and the size of the largest clone were selected for visualization.

Sequences belonging to the same clone were then collapsed, taking the most common nucleotide at each position along the consensus sequence. Clones were annotated for antibody isotypes by majority vote. IgG isotype clones were retained for further analysis of somatic hypermutation. Nucleotide mutation frequencies of each collapsed clone were calculated across the entire heavy chain sequence (with N/P and D-segment regions masked), normalizing by the length of the input sequence. To evaluate somatic hypermutation propensity, the percentage of clones with 1+ or 2+ mutations was determined in each sample and compared across experimental groups. To estimate selection pressure, the collapsed clone sequences from each experimental group

Downloaded from https://www.science.org at University of Massachusetts Worcester on January 12, 2022

(*Bcl6*$^{fl/fl}$ or *Bcl6*$^{fl/fl}$*Cd4*^{Cre}) were analyzed using BASELINe (*40*, *41*), a method that compares the observed vs expected ratios of replacement to synonymous mutations. Specifically, the observed substitution frequencies in each V segment (excluding CDR3), grouped by CDR or FWR, were compared to the expected frequencies of a reference somatic hypermutation targeting model using the "focused" test statistic. As a reference model for somatic hypermutation in murine heavy chains is not currently available, the HH_S5F human heavy chain 5-mer targeting model was used for analysis, since it has been previously been shown that human heavy vs light chains have considerably different mutational patterns (*64*). Larger BASELINe values (corresponding to an increased ratio of replacement mutations) are consistent with positive selection.

Immunofluorescence

MedLN were fixed with 4% paraformaldehyde in PBS for 4 hours at 4°C, followed by cryopreservation with 20% sucrose in PBS for 2 hours at 4°C. MedLN were snap-frozen in optimal cutting temperature compound and stored at -80°C. Tissues were cut into 7-μm sections and blocked with 10% rat serum in staining solution (PBS with 1% BSA and 0.1% Tween-20) for 1 hour at room temperature. Sections were stained with Fc block, BV421 anti-IgD (11-26c.2a; BioLegend, 405725), AF488 anti-TCRβ (H57-597; BioLegend, 109215), biotinylated anti-CD35 (8C12; BD Biosciences, 553816), and AF647 anti-GL7 (GL7; BioLegend, 144606) overnight at 4°C. Secondary staining was performed with AF594 streptavidin (BioLegend, 405240) for 1 hour at room temperature. Images were acquired on a Nikon TiE Spinning Disk Confocal Microscope with the 20× objective. Tile scan images were taken with the 20× objective with 10% overlap. Image analysis was performed with ImageJ.

Pseudovirus production

Vesicular stomatitis virus (VSV)-based pseudotyped viruses were produced as previously described (*55*, *65*). Vector pCAGGS containing the SARS-CoV-2 Wuhan-Hu-1 spike glycoprotein gene was produced under HHSN272201400008C and obtained through BEI Resources (NR-52310). The sequence of the Wuhan-Hu-1 isolate spike glycoprotein is identical to that of the USA-WA1/2020 isolate. The spike sequence of the B.1.351 variant of concern was generated by introducing the following mutations: L18F, D80A, D215G, R246I, K417N, E484K, N501Y, and A701V. 293T cells were transfected with either spike plasmid, followed by inoculation with replication-deficient VSV expressing *Renilla* luciferase for 1 hour at 37°C (*65*). The virus inoculum was then removed, and cells were washed with PBS before adding media with anti-VSV-G (8G5F11) to neutralize residual inoculum. Supernatant containing pseudovirus was collected 24 hours post inoculation, clarified by centrifugation, concentrated with Amicon Ultra Centrifugal Filter Units (100 kDa), and stored in aliquots at -80°C. Pseudoviruses were titrated in Huh7.5 cells to achieve a relative light unit (RLU) signal of 600 times the cell-only control background.

Pseudovirus neutralization assay

Sera for neutralization assay were heat-inactivated for 30 min at 56°C. Sera were tested at a starting dilution of 1:50 for USA-WA1/2020 pseudovirus and 1:12.5 for B.1.351 pseudovirus, with up to eight two-fold serial dilutions. 2×10^4 Huh7.5 cells were plated in each well of a 96-well plate the day before. Serial dilutions of sera were incubated with pseudovirus for 1 hour at 37°C. Growth media was then aspirated from the cells and replaced with 50 μl of serum/virus mixture. Luciferase activity was measured at 24 hours post infection using the *Renilla* Luciferase Assay System (Promega). Each well of cells was lysed with 50 μl Lysis Buffer, and 15 μl cell lysate was then mixed with 15 μl Luciferase Assay reagent. Luminescence was measured on a microplate reader (BioTek Synergy). Half maximal inhibitory concentration (IC50) was calculated as previously described (*66*). Neutralizing titer (NT50) was defined as the inverse of IC50.

Serum transfer

Sera from SARS-CoV-2-infected AAV-hACE2 *Bcl6*$^{fl/fl}$ or *Bcl6*$^{fl/fl}$*Cd4*^{Cre} mice at 14 days post infection (dpi) were pooled, and the resulting levels of spike-specific IgG were measured by ELISA. *Bcl6*$^{fl/fl}$ sera was left undiluted or diluted with naïve sera to match the spike-specific IgG titer of undiluted *Bcl6*$^{fl/fl}$*Cd4*^{Cre} sera. Serum samples were then mixed 1:1 with PBS, and 200 μl of serum/PBS mixture was transferred intravascularly by retro-orbital injection into K18-hACE2 mice under anesthesia with 30% isoflurane.

Measurement of lung viral burden

The left lobe of the lung was collected and homogenized in 1 ml DMEM supplemented with 2% heat-inactivated FBS and 1% Penicillin/Streptomycin. Lung homogenates were clarified by centrifugation at 3200 × *g* for 10 min and stored in aliquots at -80°C. Viral burden was measured in lung homogenates by plaque assay on Vero-E6 cells as previously described (*55*). In addition, 250 μl of lung homogenate was mixed with 750 μl of TRIzol LS Reagent (Invitrogen), and RNA was extracted with the RNeasy Mini Kit (Qiagen) following manufacturer's instructions. cDNA synthesis was performed using random hexamers and ImProm-II Reverse Transcriptase (Promega). Quantitative PCR (qPCR) was performed in triplicate for samples and standards using SARS-CoV-2 nucleocapsid (N1)-specific oligonucleotides: Probe: *5′* 6FAM-ACCCCGCATTACGTTTGGTGGACC-BHQ1 *3′*; Forward primer: *5′* GACCCCAAAATCAGCGAAAT-*3′*; Reverse primer: *5′* TCTGGTTACTGCCAGTTGAATCTG *3′*. The limit of detection was 100 SARS-CoV-2 genome copies/μl. Virus copy numbers were quantified using a control plasmid containing the complete nucleocapsid gene from SARS-CoV-2. SARS-CoV-2 genome copies were normalized to *Actb* using

Downloaded from https://www.science.org at University of Massachusetts Worcester on January 12, 2022

Actb-specific oligonucleotides: Probe: 5′ 6-JOEN-CACCAGTTC /ZEN/ GCCATGGATGACGA-IABkFQ 3′; Forward primer: 5′ GCTCCTTCGTTGCCGGTCCA 3′; Reverse primer: 5′ TTGCACATGCCGGAGCCGTT 3′. The limit of detection was 100 *Actb* copies/μl. Samples with undetectable SARS-CoV-2 genome copies were set at 0.01 relative to *Actb*.

Serum epitope repertoire analysis (SERA) with SARS-CoV-2 linear epitope library

Serum samples for epitope profiling were inactivated with UV light (250 mJ). The SERA platform for next-generation sequencing (NGS)-based analysis of antibody epitope repertoires has been previously described (*67*). In brief, *Escherichia coli* were engineered with a surface display vector carrying linear peptides derived from the SARS-CoV-2 proteome (GenBank MN908947.3), designed using oligonucleotides (Twist Bioscience) encoding peptides 12 amino acids in length and tiled with 8 amino acids overlapping. Serum samples (0.5 μl each) were then diluted 1:200 in a suspension of PBS and bacteria carrying the surface display library (10^9 cells per sample with 3×10^5 fold library representation), and incubated so that antibodies contained in the serum would bind to the peptides on the surface of the bacteria. After incubating with protein A/G magnetic beads and magnetically isolating bacteria that were bound to antibodies contained in the serum, plasmid DNA was purified and PCR amplified for NGS. Unique molecular identifiers (UMIs) were applied during PCR to minimize amplification bias, designed as an 8 base pair semi-random sequence (NNNNNNHH). After preprocessing and read trimming the raw sequencing data, the resulting reads were filtered by utilizing the UMIs to remove PCR duplicates. The filtered UMI data (hereafter referred to as reads) were then aligned to the original reference of linear epitopes derived from SARS-CoV-2 and quantified.

From the raw mapped read counts for each of the 2410 linear epitopes represented in the library, we first calculated the Shannon entropy and Simpson's diversity index of each sample using the *diversity* function in the *diverse* R package. To calculate the "repertoire focusing index", we used the formula: 1-(H'/$\log_2$(R)), where H' is Shannon entropy and R is richness, defined here as the number of unique epitopes recognized by a given sample (read count > 0). Statistical differences in these various metrics were assessed by two-tailed unpaired Welch's *t* test, comparing $Bcl6^{fl/fl}$ and $Bcl6^{fl/fl}Cd4^{Cre}$ conditions.

For further analysis, we normalized the raw count data using the median ratio approach implemented in DESeq2 (*68*). Differential enrichment analysis was performed using the Wald test in DESeq2, comparing $Bcl6^{fl/fl}$ vs $Bcl6^{fl/fl}Cd4^{Cre}$ samples. Multiple hypothesis correction was performed by the Benjamini-Hochberg method, setting a statistical significance threshold of adjusted $p < 0.05$. After identifying differentially enriched epitopes, the normalized counts were $\log_2$ transformed (hereafter referred to as $\log_2$ normalized counts) for downstream visualization and analysis.

For converting the $\log_2$ normalized counts into relative enrichment scores on a sample-by-sample basis, we scaled the $\log_2$ normalized counts within each sample to *z*-scores. In this manner, a *z*-score of 0 would correspond to epitopes that exhibited an average level of enrichment in a given sample; a positive *z*-score would indicate that an epitope is relatively enriched in a sample, while a negative *z*-score would denote a low-scoring epitope. Where applicable, statistical significance was assessed on the within-sample *z*-scores by two-tailed unpaired Welch's *t* test. For visualization purposes, we also calculated the average *z*-scores in $Bcl6^{fl/fl}$ or $Bcl6^{fl/fl}Cd4^{Cre}$ groups.

Pan-human coronavirus (hCoV) conservation scores were calculated through multiple alignment of several hCoV spike sequences using Clustal Omega. The following hCoV spike sequences were used: HKU1 (UniProt: Q0ZME7), OC43 (P36334), 229E (P15423), NL63 (Q6Q1S2), SARS-CoV (P59594), SARS-CoV-2 (P0DTC2), and MERS-CoV (K9N5Q8). Amino-acid level conservation scores for SARS-CoV-2 spike were extracted through JalView.

Statistical analysis

Data analysis was performed using GraphPad Prism 9 unless otherwise indicated. Data were analyzed using one-way ANOVA with Tukey's test or Dunnett's test; Welch's *t* test with Bonferroni multiple hypothesis correction; Student's two-tailed, unpaired *t* test; Welch's two-tailed, unpaired *t* test; two-tailed Mann–Whitney test; or two-tailed Wilcoxon signed-rank test, as indicated. $P < 0.05$ was considered statistically significant.

SUPPLEMENTARY MATERIALS

www.science.org/doi/10.1126/sciimmunol.abl5652
Figs. S1 to S7
Data files S1 to S3
MDAR Reproducibility Checklist

REFERENCES AND NOTES

1. K. McMahan, J. Yu, N. B. Mercado, C. Loos, L. H. Tostanoski, A. Chandrashekar, J. Liu, L. Peter, C. Atyeo, A. Zhu, E. A. Bondzie, G. Dagotto, M. S. Gebre, C. Jacob-Dolan, Z. Li, F. Nampanya, S. Patel, L. Pessaint, A. Van Ry, K. Blade, J. Yalley-Ogunro, M. Cabus, R. Brown, A. Cook, E. Teow, H. Andersen, M. G. Lewis, D. A. Lauffenburger, G. Alter, D. H. Barouch, Correlates of protection against SARS-CoV-2 in rhesus macaques. *Nature* **590**, 630–634 (2021). doi:10.1038/s41586-020-03041-6 Medline
2. S. Crotty, T Follicular Helper Cell Biology: A Decade of Discovery and Diseases. *Immunity* **50**, 1132–1148 (2019). doi:10.1016/j.immuni.2019.04.011 Medline
3. D. Baumjohann, N. Fazilleau, Antigen-dependent multistep differentiation of T follicular helper cells and its role in SARS-CoV-2 infection and vaccination. *Eur. J. Immunol.* **51**, 1325–1333 (2021). doi:10.1002/eji.202049148 Medline
4. J. Zhang, Q. Wu, Z. Liu, Q. Wang, J. Wu, Y. Hu, T. Bai, T. Xie, M. Huang, T. Wu, D. Peng, W. Huang, K. Jin, L. Niu, W. Guo, D. Luo, D. Lei, Z. Wu, G. Li, R. Huang, Y. Lin, X. Xie, S. He, Y. Deng, J. Liu, W. Li, Z. Lu, H. Chen, T. Zeng, Q. Luo, Y.-P. Li, Y. Wang, W. Liu, X. Qu, Spike-specific circulating T follicular helper cell and cross-neutralizing antibody responses in COVID-19-convalescent individuals. *Nat. Microbiol.* **6**, 51–58 (2021). doi:10.1038/s41564-020-00824-5 Medline
5. C. Rydyznski Moderbacher, S. I. Ramirez, J. M. Dan, A. Grifoni, K. M. Hastie, D.

Downloaded from https://www.science.org at University of Massachusetts Worcester on January 12, 2022

Weiskopf, S. Belanger, R. K. Abbott, C. Kim, J. Choi, Y. Kato, E. G. Crotty, C. Kim, S. A. Rawlings, J. Mateus, L. P. V. Tse, A. Frazier, R. Baric, B. Peters, J. Greenbaum, E. Ollmann Saphire, D. M. Smith, A. Sette, S. Crotty, Antigen-Specific Adaptive Immunity to SARS-CoV-2 in Acute COVID-19 and Associations with Age and Disease Severity. *Cell* **183**, 996–1012.e19 (2020). doi:10.1016/j.cell.2020.09.038 Medline

6. N. Kaneko, H.-H. Kuo, J. Boucau, J. R. Farmer, H. Allard-Chamard, V. S. Mahajan, A. Piechocka-Trocha, K. Lefteri, M. Osborn, J. Bals, Y. C. Bartsch, N. Bonheur, T. M. Caradonna, J. Chevalier, F. Chowdhury, T. J. Diefenbach, K. Einkauf, J. Fallon, J. Feldman, K. K. Finn, P. Garcia-Broncano, C. A. Hartana, B. M. Hauser, C. Jiang, P. Kaplonek, M. Karpell, E. C. Koscher, X. Lian, H. Liu, J. Liu, N. L. Ly, A. R. Michell, Y. Rassadkina, K. Seiger, L. Sessa, S. Shin, N. Singh, W. Sun, X. Sun, H. J. Ticheli, M. T. Waring, A. L. Zhu, G. Alter, J. Z. Li, D. Lingwood, A. G. Schmidt, M. Lichterfeld, B. D. Walker, X. G. Yu, R. F. Padera, S. Pillai, Loss of Bcl-6-Expressing T Follicular Helper Cells and Germinal Centers in COVID-19. *Cells*, 0092867420310679 (2020).
7. Y. Q. Duan, M. H. Xia, L. Ren, Y. F. Zhang, Q. L. Ao, S. P. Xu, D. Kuang, Q. Liu, B. Yan, Y. W. Zhou, Q. Chu, L. Liu, X.-P. Yang, G. P. Wang, Deficiency of Tfh Cells and Germinal Center in Deceased COVID-19 Patients. *Curr. Med. Sci.* **40**, 618–624 (2020). doi:10.1007/s11596-020-2225-x Medline
8. M. C. Woodruff, R. P. Ramonell, D. C. Nguyen, K. S. Cashman, A. S. Saini, N. S. Haddad, A. M. Ley, S. Kyu, J. C. Howell, T. Ozturk, S. Lee, N. Suryadevara, J. B. Case, R. Bugrovsky, W. Chen, J. Estrada, A. Morrison-Porter, A. Derrico, F. A. Anam, M. Sharma, H. M. Wu, S. N. Le, S. A. Jenks, C. M. Tipton, B. Staitieh, J. L. Daiss, E. Ghosn, M. S. Diamond, R. H. Carnahan, J. E. Crowe Jr., W. T. Hu, F. E.-H. Lee, I. Sanz, Extrafollicular B cell responses correlate with neutralizing antibodies and morbidity in COVID-19. *Nat. Immunol.* **21**, 1506–1516 (2020). doi:10.1038/s41590-020-00814-z Medline
9. J. Chen, Y. F. Lau, E. W. Lamirande, C. D. Paddock, J. H. Bartlett, S. R. Zaki, K. Subbarao, Cellular immune responses to severe acute respiratory syndrome coronavirus (SARS-CoV) infection in senescent BALB/c mice: CD4+ T cells are important in control of SARS-CoV infection. *J. Virol.* **84**, 1289–1301 (2010). doi:10.1128/JVI.01281-09 Medline
10. S. Crotty, E. N. Kersh, J. Cannons, P. L. Schwartzberg, R. Ahmed, SAP is required for generating long-term humoral immunity. *Nature* **421**, 282–287 (2003). doi:10.1038/nature01318 Medline
11. C. Kamperschroer, J. P. Dibble, D. L. Meents, P. L. Schwartzberg, S. L. Swain, SAP is required for Th cell function and for immunity to influenza. *J. Immunol.* **177**, 5317–5327 (2006). doi:10.4049/jimmunol.177.8.5317 Medline
12. L. M. Fahey, E. B. Wilson, H. Elsaesser, C. D. Fistonich, D. B. McGavern, D. G. Brooks, Viral persistence redirects CD4 T cell differentiation toward T follicular helper cells. *J. Exp. Med.* **208**, 987–999 (2011). doi:10.1084/jem.20101773 Medline
13. X. Liu, X. Chen, B. Zhong, A. Wang, X. Wang, F. Chu, R. I. Nurieva, X. Yan, P. Chen, L. G. van der Flier, H. Nakatsukasa, S. S. Neelapu, W. Chen, H. Clevers, Q. Tian, H. Qi, L. Wei, C. Dong, Transcription factor achaete-scute homologue 2 initiates follicular T-helper-cell development. *Nature* **507**, 513–518 (2014). doi:10.1038/nature12910 Medline
14. J. P. Ray, H. D. Marshall, B. J. Laidlaw, M. M. Staron, S. M. Kaech, J. Craft, Transcription factor STAT3 and type I interferons are corepressive insulators for differentiation of follicular helper and T helper 1 cells. *Immunity* **40**, 367–377 (2014). doi:10.1016/j.immuni.2014.02.005 Medline
15. U. Greczmiel, N. J. Kräutler, A. Pedrioli, I. Bartsch, P. Agnellini, G. Bedenikovic, J. Harker, K. Richter, A. Oxenius, Sustained T follicular helper cell response is essential for control of chronic viral infection. *Sci. Immunol.* **2**, eaam8686 (2017). doi:10.1126/sciimmunol.aam8686 Medline
16. G. Xin, R. Zander, D. M. Schauder, Y. Chen, J. S. Weinstein, W. R. Drobyski, V. Tarakanova, J. Craft, W. Cui, Single-cell RNA sequencing unveils an IL-10-producing helper subset that sustains humoral immunity during persistent infection. *Nat. Commun.* **9**, 5037 (2018). doi:10.1038/s41467-018-07492-4 Medline
17. H. Liang, J. Tang, Z. Liu, Y. Liu, Y. Huang, Y. Xu, P. Hao, Z. Yin, J. Zhong, L. Ye, X. Jin, H. Wang, ZIKV infection induces robust Th1-like Tfh cell and long-term protective antibody responses in immunocompetent mice. *Nat. Commun.* **10**, 3859 (2019). doi:10.1038/s41467-019-11754-0 Medline
18. S. K. Lee, R. J. Rigby, D. Zotos, L. M. Tsai, S. Kawamoto, J. L. Marshall, R. R. Ramiscal, T. D. Chan, D. Gatto, R. Brink, D. Yu, S. Fagarasan, D. M. Tarlinton, A. F. Cunningham, C. G. Vinuesa, B cell priming for extrafollicular antibody responses requires Bcl-6 expression by T cells. *J. Exp. Med.* **208**, 1377–1388 (2011). doi:10.1084/jem.20102065 Medline
19. K. Miyauchi, A. Sugimoto-Ishige, Y. Harada, Y. Adachi, Y. Usami, T. Kaji, K. Inoue, H. Hasegawa, T. Watanabe, A. Hijikata, S. Fukuyama, T. Maemura, M. Okada-Hatakeyama, O. Ohara, Y. Kawaoka, Y. Takahashi, T. Takemori, M. Kubo, Protective neutralizing influenza antibody response in the absence of T follicular helper cells. *Nat. Immunol.* **17**, 1447–1458 (2016). doi:10.1038/ni.3563 Medline
20. J. A. Kotov, M. K. Jenkins, Cutting Edge: T Cell-Dependent Plasmablasts Form in the Absence of Single Differentiated CD4$^+$ T Cell Subsets. *J. Immunol.* **202**, 401–405 (2019). doi:10.4049/jimmunol.1801349 Medline
21. T. Junt, K. Fink, R. Förster, B. Senn, M. Lipp, M. Muramatsu, R. M. Zinkernagel, B. Ludewig, H. Hengartner, CXCR5-dependent seeding of follicular niches by B and Th cells augments antiviral B cell responses. *J. Immunol.* **175**, 7109–7116 (2005). doi:10.4049/jimmunol.175.11.7109 Medline
22. K. Hollister, S. Kusam, H. Wu, N. Clegg, A. Mondal, D. V. Sawant, A. L. Dent, Insights into the role of Bcl6 in follicular Th cells using a new conditional mutant mouse model. *J. Immunol.* **191**, 3705–3711 (2013). doi:10.4049/jimmunol.1300378 Medline
23. H. Toyama, S. Okada, M. Hatano, Y. Takahashi, N. Takeda, H. Ichii, T. Takemori, Y. Kuroda, T. Tokuhisa, Memory B cells without somatic hypermutation are generated from Bcl6-deficient B cells. *Immunity* **17**, 329–339 (2002). doi:10.1016/S1074-7613(02)00387-4 Medline
24. S.-E. Bentebibel, S. Lopez, G. Obermoser, N. Schmitt, C. Mueller, C. Harrod, E. Flano, A. Mejias, R. A. Albrecht, D. Blankenship, H. Xu, V. Pascual, J. Banchereau, A. Garcia-Sastre, A. K. Palucka, O. Ramilo, H. Ueno, Induction of ICOS+CXCR3+CXCR5+ TH cells correlates with antibody responses to influenza vaccination. *Sci. Transl. Med.* **5**, 176ra32 (2013). doi:10.1126/scitranslmed.3005191 Medline
25. F. Spensieri, E. Borgogni, L. Zedda, M. Bardelli, F. Buricchi, G. Volpini, E. Fragapane, S. Tavarini, O. Finco, R. Rappuoli, G. Del Giudice, G. Galli, F. Castellino, Human circulating influenza-CD4+ ICOS1+IL-21+ T cells expand after vaccination, exert helper function, and predict antibody responses. *Proc. Natl. Acad. Sci. U.S.A.* **110**, 14330–14335 (2013). doi:10.1073/pnas.1311998110 Medline
26. T. Kobayashi, K. Iijima, A. L. Dent, H. Kita, Follicular helper T cells mediate IgE antibody response to airborne allergens. *J. Allergy Clin. Immunol.* **139**, 300–313.e7 (2017). doi:10.1016/j.jaci.2016.04.021 Medline
27. C.-H. Chang, S. Guerder, S.-C. Hong, W. van Ewijk, R. A. Flavell, Mice lacking the MHC class II transactivator (CIITA) show tissue-specific impairment of MHC class II expression. *Immunity* **4**, 167–178 (1996). doi:10.1016/S1074-7613(00)80681-0 Medline
28. P. Zhou, X.-L. Yang, X.-G. Wang, B. Hu, L. Zhang, W. Zhang, H.-R. Si, Y. Zhu, B. Li, C.-L. Huang, H.-D. Chen, J. Chen, Y. Luo, H. Guo, R.-D. Jiang, M.-Q. Liu, Y. Chen, X.-R. Shen, X. Wang, X.-S. Zheng, K. Zhao, Q.-J. Chen, F. Deng, L.-L. Liu, B. Yan, F.-X. Zhan, Y.-Y. Wang, G.-F. Xiao, Z.-L. Shi, A pneumonia outbreak associated with a new coronavirus of probable bat origin. *Nature* **579**, 270–273 (2020). doi:10.1038/s41586-020-2012-7 Medline
29. B. Israelow, E. Song, T. Mao, P. Lu, A. Meir, F. Liu, M. M. Alfajaro, J. Wei, H. Dong, R. J. Homer, A. Ring, C. B. Wilen, A. Iwasaki, Mouse model of SARS-CoV-2 reveals inflammatory role of type I interferon signaling. *J. Exp. Med.* **217**, e20201241 (2020). doi:10.1084/jem.20201241 Medline
30. P. B. McCray Jr., L. Pewe, C. Wohlford-Lenane, M. Hickey, L. Manzel, L. Shi, J. Netland, H. P. Jia, C. Halabi, C. D. Sigmund, D. K. Meyerholz, P. Kirby, D. C. Look, S. Perlman, Lethal infection of K18-hACE2 mice infected with severe acute respiratory syndrome coronavirus. *J. Virol.* **81**, 813–821 (2007). doi:10.1128/JVI.02012-06 Medline
31. W. Dejnirattisai, D. Zhou, H. M. Ginn, H. M. E. Duyvesteyn, P. Supasa, J. B. Case, Y. Zhao, T. S. Walter, A. J. Mentzer, C. Liu, B. Wang, G. C. Paesen, J. Slon-Campos, C. López-Camacho, N. M. Kafai, A. L. Bailey, R. E. Chen, B. Ying, C. Thompson, J. Bolton, A. Fyfe, S. Gupta, T. K. Tan, J. Gilbert-Jaramillo, W. James, M. Knight, M. W. Carroll, D. Skelly, C. Dold, Y. Peng, R. Levin, T. Dong, A. J. Pollard, J. C. Knight, P. Klenerman, N. Temperton, D. R. Hall, M. A. Williams, N. G. Paterson, F. K. R. Bertram, C. A. Siebert, D. K. Clare, A. Howe, J. Radecke, Y. Song, A. R. Townsend,

Downloaded from https://www.science.org at University of Massachusetts Worcester on January 12, 2022

K. A. Huang, E. E. Fry, J. Mongkolsapaya, M. S. Diamond, J. Ren, D. I. Stuart, G. R. Screaton, The antigenic anatomy of SARS-CoV-2 receptor binding domain. *Cell* **184**, 2183–2200.e22 (2021). doi:10.1016/j.cell.2021.02.032 Medline

32. P. J. M. Brouwer, T. G. Caniels, K. van der Straten, J. L. Snitselaar, Y. Aldon, S. Bangaru, J. L. Torres, N. M. A. Okba, M. Claireaux, G. Kerster, A. E. H. Bentlage, M. M. van Haaren, D. Guerra, J. A. Burger, E. E. Schermer, K. D. Verheul, N. van der Velde, A. van der Kooi, J. van Schooten, M. J. van Breemen, T. P. L. Bijl, K. Sliepen, A. Aartse, R. Derking, I. Bontjer, N. A. Kootstra, W. J. Wiersinga, G. Vidarsson, B. L. Haagmans, A. B. Ward, G. J. de Bree, R. W. Sanders, M. J. van Gils, Potent neutralizing antibodies from COVID-19 patients define multiple targets of vulnerability. *Science* **369**, 643–650 (2020). doi:10.1126/science.abc5902 Medline
33. D. F. Robbiani, C. Gaebler, F. Muecksch, J. C. C. Lorenzi, Z. Wang, A. Cho, M. Agudelo, C. O. Barnes, A. Gazumyan, S. Finkin, T. Hägglöf, T. Y. Oliveira, C. Viant, A. Hurley, H.-H. Hoffmann, K. G. Millard, R. G. Kost, M. Cipolla, K. Gordon, F. Bianchini, S. T. Chen, V. Ramos, R. Patel, J. Dizon, I. Shimeliovich, P. Mendoza, H. Hartweger, L. Nogueira, M. Pack, J. Horowitz, F. Schmidt, Y. Weisblum, E. Michailidis, A. W. Ashbrook, E. Waltari, J. E. Pak, K. E. Huey-Tubman, N. Koranda, P. R. Hoffman, A. P. West Jr., C. M. Rice, T. Hatziioannou, P. J. Bjorkman, P. D. Bieniasz, M. Caskey, M. C. Nussenzweig, Convergent antibody responses to SARS-CoV-2 in convalescent individuals. *Nature* **584**, 437–442 (2020). doi:10.1038/s41586-020-2456-9 Medline
34. M. Yuan, H. Liu, N. C. Wu, C. D. Lee, X. Zhu, F. Zhao, D. Huang, W. Yu, Y. Hua, H. Tien, T. F. Rogers, E. Landais, D. Sok, J. G. Jardine, D. R. Burton, I. A. Wilson, Structural basis of a shared antibody response to SARS-CoV-2. *Science* **369**, 1119–1123 (2020). doi:10.1126/science.abd2321 Medline
35. L. Wang, T. Zhou, Y. Zhang, E. S. Yang, C. A. Schramm, W. Shi, A. Pegu, O. K. Oloniniyi, A. R. Henry, S. Darko, S. R. Narpala, C. Hatcher, D. R. Martinez, Y. Tsybovsky, E. Phung, O. M. Abiona, A. Antia, E. M. Cale, L. A. Chang, M. Choe, K. S. Corbett, R. L. Davis, A. T. DiPiazza, I. J. Gordon, S. H. Hait, T. Hermanus, P. Kgagudi, F. Laboune, K. Leung, T. Liu, R. D. Mason, A. F. Nazzari, L. Novik, S. O'Connell, S. O'Dell, A. S. Olia, S. D. Schmidt, T. Stephens, C. D. Stringham, C. A. Talana, I.-T. Teng, D. A. Wagner, A. T. Widge, B. Zhang, M. Roederer, J. E. Ledgerwood, T. J. Ruckwardt, M. R. Gaudinski, P. L. Moore, N. A. Doria-Rose, R. S. Baric, B. S. Graham, A. B. McDermott, D. C. Douek, P. D. Kwong, J. R. Mascola, N. J. Sullivan, J. Misasi, Ultrapotent antibodies against diverse and highly transmissible SARS-CoV-2 variants. *Science* **373**, eabh1766 (2021). doi:10.1126/science.abh1766 Medline
36. J. Feldman, J. Bals, C. G. Altomare, K. St Denis, E. C. Lam, B. M. Hauser, L. Ronsard, M. Sangesland, T. B. Moreno, V. Okonkwo, N. Hartojo, A. B. Balazs, G. Bajic, D. Lingwood, A. G. Schmidt, Naive human B cells engage the receptor binding domain of SARS-CoV-2, variants of concern, and related sarbecoviruses. *Sci. Immunol.* **6**, eabl5842 (2021). doi:10.1126/sciimmunol.abl5842 Medline
37. R. Di Niro, S.-J. Lee, J. A. Vander Heiden, R. A. Elsner, N. Trivedi, J. M. Bannock, N. T. Gupta, S. H. Kleinstein, F. Vigneault, T. J. Gilbert, E. Meffre, S. J. McSorley, M. J. Shlomchik, Salmonella Infection Drives Promiscuous B Cell Activation Followed by Extrafollicular Affinity Maturation. *Immunity* **43**, 120–131 (2015). doi:10.1016/j.immuni.2015.06.013 Medline
38. N. Trivedi, F. Weisel, S. Smita, S. Joachim, M. Kader, A. Radhakrishnan, C. Clouser, A. M. Rosenfeld, M. Chikina, F. Vigneault, U. Hershberg, N. Ismail, M. J. Shlomchik, Liver Is a Generative Site for the B Cell Response to Ehrlichia muris. *Immunity* **51**, 1088–1101.e5 (2019). doi:10.1016/j.immuni.2019.10.004 Medline
39. J. William, C. Euler, S. Christensen, M. J. Shlomchik, Evolution of autoantibody responses via somatic hypermutation outside of germinal centers. *Science* **297**, 2066–2070 (2002). doi:10.1126/science.1073924 Medline
40. G. Yaari, M. Uduman, S. H. Kleinstein, Quantifying selection in high-throughput Immunoglobulin sequencing data sets. *Nucleic Acids Res.* **40**, e134 (2012). doi:10.1093/nar/gks457 Medline
41. G. Yaari, J. A. Vander Heiden, M. Uduman, D. Gadala-Maria, N. Gupta, J. N. H. Stern, K. C. O'Connor, D. A. Hafler, U. Laserson, F. Vigneault, S. H. Kleinstein, Models of somatic hypermutation targeting and substitution based on synonymous mutations from high-throughput immunoglobulin sequencing data. *Front. Immunol.* **4**, 358 (2013). doi:10.3389/fimmu.2013.00358 Medline
42. M. A. Tortorici, D. Veesler, in *Advances in Virus Research*, F. A. Rey, Ed. (Academic Press, 2019; https://www.sciencedirect.com/science/article/pii/S0065352719300284), vol. 105 of *Complementary Strategies to Understand Virus Structure and Function*, pp. 93–116.
43. J. T. Ladner, S. N. Henson, A. S. Boyle, A. L. Engelbrektson, Z. W. Fink, F. Rahee, J. D'ambrozio, K. E. Schaecher, M. Stone, W. Dong, S. Dadwal, J. Yu, M. A. Caligiuri, P. Cieplak, M. Bjørås, M. H. Fenstad, S. A. Nordbø, D. E. Kainov, N. Muranaka, M. S. Chee, S. A. Shiryaev, J. A. Altin, Epitope-resolved profiling of the SARS-CoV-2 antibody response identifies cross-reactivity with endemic human coronaviruses. *CR Med* **2**, 100189 (2021). doi:10.1016/j.xcrm.2020.100189 Medline
44. Y. Li, M. L. Ma, Q. Lei, F. Wang, W. Hong, D. Y. Lai, H. Hou, Z. W. Xu, B. Zhang, H. Chen, C. Yu, J. B. Xue, Y. X. Zheng, X. N. Wang, H. W. Jiang, H. N. Zhang, H. Qi, S. J. Guo, Y. Zhang, X. Lin, Z. Yao, J. Wu, H. Sheng, Y. Zhang, H. Wei, Z. Sun, X. Fan, S. C. Tao, Linear epitope landscape of the SARS-CoV-2 Spike protein constructed from 1,051 COVID-19 patients. *Cell Rep.* **34**, 108915 (2021). doi:10.1016/j.celrep.2021.108915 Medline
45. M. Hoffmann, P. Arora, R. Groß, A. Seidel, B. F. Hörnich, A. S. Hahn, N. Krüger, L. Graichen, H. Hofmann-Winkler, A. Kempf, M. S. Winkler, S. Schulz, H.-M. Jäck, B. Jahrsdörfer, H. Schrezenmeier, M. Müller, A. Kleger, J. Münch, S. Pöhlmann, SARS-CoV-2 variants B.1.351 and P.1 escape from neutralizing antibodies. *Cell* **184**, 2384–2393.e12 (2021). doi:10.1016/j.cell.2021.03.036 Medline
46. D. Zhou, W. Dejnirattisai, P. Supasa, C. Liu, A. J. Mentzer, H. M. Ginn, Y. Zhao, H. M. E. Duyvesteyn, A. Tuekprakhon, R. Nutalai, B. Wang, G. C. Paesen, C. Lopez-Camacho, J. Slon-Campos, B. Hallis, N. Coombes, K. Bewley, S. Charlton, T. S. Walter, D. Skelly, S. F. Lumley, C. Dold, R. Levin, T. Dong, A. J. Pollard, J. C. Knight, D. Crook, T. Lambe, E. Clutterbuck, S. Bibi, A. Flaxman, M. Bittaye, S. Belij-Rammerstorfer, S. Gilbert, W. James, M. W. Carroll, P. Klenerman, E. Barnes, S. J. Dunachie, E. E. Fry, J. Mongkolsapaya, J. Ren, D. I. Stuart, G. R. Screaton, Evidence of escape of SARS-CoV-2 variant B.1.351 from natural and vaccine-induced sera. *Cell* **184**, 2348–2361.e6 (2021). doi:10.1016/j.cell.2021.02.037 Medline
47. A. Mendoza, W. T. Yewdell, B. Hoyos, M. Schizas, R. Bou-Puerto, A. J. Michaels, C. C. Brown, J. Chaudhuri, A. Y. Rudensky, Assembly of a spatial circuit of T-bet-expressing T and B lymphocytes is required for antiviral humoral immunity. *Sci. Immunol.* **6**, eabi4710 (2021). doi:10.1126/sciimmunol.abi4710 Medline
48. S. C. Eisenbarth, D. Baumjohann, J. Craft, N. Fazilleau, C. S. Ma, S. G. Tangye, C. G. Vinuesa, M. A. Linterman, CD4$^+$ T cells that help B cells - a proposal for uniform nomenclature. *Trends Immunol.* **42**, 658–669 (2021). doi:10.1016/j.it.2021.06.003 Medline
49. B. O. Lee, J. Rangel-Moreno, J. E. Moyron-Quiroz, L. Hartson, M. Makris, F. Sprague, F. E. Lund, T. D. Randall, CD4 T cell-independent antibody response promotes resolution of primary influenza infection and helps to prevent reinfection. *J. Immunol.* **175**, 5827–5838 (2005). doi:10.4049/jimmunol.175.9.5827 Medline
50. D. Pinto, M. M. Sauer, N. Czudnochowski, J. S. Low, M. A. Tortorici, M. P. Housley, J. Noack, A. C. Walls, J. E. Bowen, B. Guarino, L. E. Rosen, J. di Iulio, J. Jerak, H. Kaiser, S. Islam, S. Jaconi, N. Sprugasci, K. Culap, R. Abdelnabi, C. Foo, L. Coelmont, I. Bartha, S. Bianchi, C. Silacci-Fregni, J. Bassi, R. Marzi, E. Vetti, A. Cassotta, A. Ceschi, P. Ferrari, P. E. Cippà, O. Giannini, S. Ceruti, C. Garzoni, A. Riva, F. Benigni, E. Cameroni, L. Piccoli, M. S. Pizzuto, M. Smithey, D. Hong, A. Telenti, F. A. Lempp, J. Neyts, C. Havenar-Daughton, A. Lanzavecchia, F. Sallusto, G. Snell, H. W. Virgin, M. Beltramello, D. Corti, D. Veesler, Broad betacoronavirus neutralization by a stem helix-specific human antibody. *Science* **373**, 1109–1116 (2021). doi:10.1126/science.abj3321 Medline
51. C.-L. Hsieh, A. P. Werner, S. R. Leist, L. J. Stevens, E. Falconer, J. A. Goldsmith, C.-W. Chou, O. M. Abiona, A. West, K. Westendorf, K. Muthuraman, E. J. Fritch, K. H. Dinnon 3rd, A. Schäfer, M. R. Denison, J. D. Chappell, R. S. Baric, B. S. Graham, K. S. Corbett, J. S. McLellan, Stabilized coronavirus spike stem elicits a broadly protective antibody. *Cell Rep.* **37**, 109929 (2021). doi:10.1016/j.celrep.2021.109929 Medline
52. R. Keating, T. Hertz, M. Wehenkel, T. L. Harris, B. A. Edwards, J. L. McClaren, S. A. Brown, S. Surman, Z. S. Wilson, P. Bradley, J. Hurwitz, H. Chi, P. C. Doherty, P. G. Thomas, M. A. McGargill, The kinase mTOR modulates the antibody response to provide cross-protective immunity to lethal infection with influenza virus. *Nat. Immunol.* **14**, 1266–1276 (2013). doi:10.1038/ni.2741 Medline
53. M. A. Linterman, How T follicular helper cells and the germinal centre response change with age. *Immunol. Cell Biol.* **92**, 72–79 (2014). doi:10.1038/icb.2013.77

Downloaded from https://www.science.org at University of Massachusetts Worcester on January 12, 2022

Medline
54. P. P. Lee, D. R. Fitzpatrick, C. Beard, H. K. Jessup, S. Lehar, K. W. Makar, M. Pérez-Melgosa, M. T. Sweetser, M. S. Schlissel, S. Nguyen, S. R. Cherry, J. H. Tsai, S. M. Tucker, W. M. Weaver, A. Kelso, R. Jaenisch, C. B. Wilson, A critical role for Dnmt1 and DNA methylation in T cell development, function, and survival. *Immunity* **15**, 763–774 (2001). doi:10.1016/S1074-7613(01)00227-8 Medline
55. J. Wei, M. M. Alfajaro, P. C. DeWeirdt, R. E. Hanna, W. J. Lu-Culligan, W. L. Cai, M. S. Strine, S.-M. Zhang, V. R. Graziano, C. O. Schmitz, J. S. Chen, M. C. Mankowski, R. B. Filler, N. G. Ravindra, V. Gasque, F. J. de Miguel, A. Patil, H. Chen, K. Y. Oguntuyo, L. Abriola, Y. V. Surovtseva, R. C. Orchard, B. Lee, B. D. Lindenbach, K. Politi, D. van Dijk, C. Kadoch, M. D. Simon, Q. Yan, J. G. Doench, C. B. Wilen, Genome-wide CRISPR Screens Reveal Host Factors Critical for SARS-CoV-2 Infection. *Cell* **184**, 76–91.e13 (2020). doi:10.1016/j.cell.2020.10.028 Medline
56. P. S. Pillai, R. D. Molony, K. Martinod, H. Dong, I. K. Pang, M. C. Tal, A. G. Solis, P. Bielecki, S. Mohanty, M. Trentalange, R. J. Homer, R. A. Flavell, D. D. Wagner, R. R. Montgomery, A. C. Shaw, P. Staeheli, A. Iwasaki, Mx1 reveals innate pathways to antiviral resistance and lethal influenza disease. *Science* **352**, 463–466 (2016). doi:10.1126/science.aaf3926 Medline
57. A. C. Walls, Y.-J. Park, M. A. Tortorici, A. Wall, A. T. McGuire, D. Veesler, Structure, Function, and Antigenicity of the SARS-CoV-2 Spike Glycoprotein. *Cell* **181**, 281–292.e6 (2020). doi:10.1016/j.cell.2020.02.058 Medline
58. Y. Chen, A. Zuiani, S. Fischinger, J. Mullur, C. Atyeo, M. Travers, F. J. N. Lelis, K. M. Pullen, H. Martin, P. Tong, A. Gautam, S. Habibi, J. Bensko, D. Gakpo, J. Feldman, B. M. Hauser, T. M. Caradonna, Y. Cai, J. S. Burke, J. Lin, J. A. Lederer, E. C. Lam, C. L. Lavine, M. S. Seaman, B. Chen, A. G. Schmidt, A. B. Balazs, D. A. Lauffenburger, G. Alter, D. R. Wesemann, Quick COVID-19 Healers Sustain Anti-SARS-CoV-2 Antibody Production. *Cell* **183**, 1496–1507.e16 (2020). doi:10.1016/j.cell.2020.10.051 Medline
59. J. A. Vander Heiden, G. Yaari, M. Uduman, J. N. H. Stern, K. C. O'Connor, D. A. Hafler, F. Vigneault, S. H. Kleinstein, pRESTO: A toolkit for processing high-throughput sequencing raw reads of lymphocyte receptor repertoires. *Bioinformatics* **30**, 1930–1932 (2014). doi:10.1093/bioinformatics/btu138 Medline
60. N. T. Gupta, J. A. Vander Heiden, M. Uduman, D. Gadala-Maria, G. Yaari, S. H. Kleinstein, Change-O: A toolkit for analyzing large-scale B cell immunoglobulin repertoire sequencing data. *Bioinformatics* **31**, 3356–3358 (2015). doi:10.1093/bioinformatics/btv359 Medline
61. N. Nouri, S. H. Kleinstein, Somatic hypermutation analysis for improved identification of B cell clonal families from next-generation sequencing data. *PLOS Comput. Biol.* **16**, e1007977 (2020). doi:10.1371/journal.pcbi.1007977 Medline
62. M. I. J. Raybould, A. Kovaltsuk, C. Marks, C. M. Deane, CoV-AbDab: The coronavirus antibody database. *Bioinformatics* **37**, 734–735 (2021). doi:10.1093/bioinformatics/btaa739 Medline
63. K. B. Hoehn, O. G. Pybus, S. H. Kleinstein, "Phylogenetic analysis of migration, differentiation, and class switching in B cells" (2020), p. 2020.05.30.124446,, doi:10.1101/2020.05.30.124446.
64. A. Cui, R. Di Niro, J. A. Vander Heiden, A. W. Briggs, K. Adams, T. Gilbert, K. C. O'Connor, F. Vigneault, M. J. Shlomchik, S. H. Kleinstein, A Model of Somatic Hypermutation Targeting in Mice Based on High-Throughput Ig Sequencing Data. *J. Immunol.* **197**, 3566–3574 (2016). doi:10.4049/jimmunol.1502263 Medline
65. V. A. Avanzato, K. Y. Oguntuyo, M. Escalera-Zamudio, B. Gutierrez, M. Golden, S. L. Kosakovsky Pond, R. Pryce, T. S. Walter, J. Seow, K. J. Doores, O. G. Pybus, V. J. Munster, B. Lee, T. A. Bowden, A structural basis for antibody-mediated neutralization of Nipah virus reveals a site of vulnerability at the fusion glycoprotein apex. *Proc. Natl. Acad. Sci. U.S.A.* **116**, 25057–25067 (2019). doi:10.1073/pnas.1912503116 Medline
66. J. M. Decker, F. Bibollet-Ruche, X. Wei, S. Wang, D. N. Levy, W. Wang, E. Delaporte, M. Peeters, C. A. Derdeyn, S. Allen, E. Hunter, M. S. Saag, J. A. Hoxie, B. H. Hahn, P. D. Kwong, J. E. Robinson, G. M. Shaw, Antigenic conservation and immunogenicity of the HIV coreceptor binding site. *J. Exp. Med.* **201**, 1407–1419 (2005). doi:10.1084/jem.20042510 Medline
67. K. Kamath, J. Reifert, T. Johnston, C. Gable, R. J. Pantazes, H. N. Rivera, I. McAuliffe, S. Handali, P. S. Daugherty, Antibody epitope repertoire analysis enables rapid antigen discovery and multiplex serology. *Sci. Rep.* **10**, 5294 (2020). doi:10.1038/s41598-020-62256-9 Medline
68. M. I. Love, W. Huber, S. Anders, Moderated estimation of fold change and dispersion for RNA-seq data with DESeq2. *Genome Biol.* **15**, 550 (2014). doi:10.1186/s13059-014-0550-8 Medline

Acknowledgments: We thank all members of the Eisenbarth and Wilen labs for helpful discussions. We would like to acknowledge Benhur Lee, Ann Haberman, Joao Pereira, Jonathan Klein, Steven Kleinstein, Kenneth Hoehn, Ruoyi Jiang, Minh Pham, Joerg Nikolaus, Yale West Campus Imaging Core, Yale Center for Genome Analysis, and BEI Resources for providing critical reagents, resources, and expertise. We thank Yale Environmental Health and Safety for providing necessary training and support for SARS-CoV-2 research. Illustrations were created with BioRender.com. **Funding:** This study was supported by National Institutes of Health grants T32GM136651 (JSC, RDC, ES), F30HL149151 (JSC), F30CA250249 (RDC), F30CA239444 (ES), T32AI007019 (TM), T32AI007517 (BI), R37AR040072 and R01AR074545 (JC), K08AI128043 and R01AI148467 (CBW), and R01AI136942 (SCE); Edward L. Tatum Fellowship from the Graduate School of Arts & Sciences and the Gershon-Trudeau Fellowship from the Department of Immunobiology of Yale University (WS); Bill & Melinda Gates Foundation (LC); DoD grant IIAR W81XWH-21-1-0019 (SC); Burroughs Wellcome Fund Career Award for Medical Scientists (CBW); Mathers Charitable Foundation (CBW); Ludwig Family Foundation (CBW); and Emergent Ventures Fast Grants (CBW, SCE). **Author contributions:** Conceptualization: JSC, CBW, SCE. Methodology: ES, TM, BI, KK, JB, WAH, JW, MMA, WS, JSW. Investigation: JSC, ES, TM, KK, JB, RBF, BLM, WS. Validation: JSC, RDC, ES, TM, KK, JB, WAH. Formal Analysis: JSC, RDC, WAH. Visualization: JSC, RDC. Resources: LP, LC, SC, JC, JCS, AI, CBW, SCE. Writing: JSC, RDC, CBW, SCE. Supervision: JSW, UG, CBW, SCE. Funding acquisition: CBW, SCE. **Competing interests:** KK, JB, WAH, and JCS declare the following competing interests: ownership of stocks or shares at Serimmune, paid employment at Serimmune, and patent applications on behalf of Serimmune. Yale University (CBW) has a patent pending entitled "Compounds and Compositions for Treating, Ameliorating, and/or Preventing SARS-CoV-2 Infection and/or Complications Thereof." **Data and materials availability:** BCR sequencing data are available via the Gene Expression Omnibus (GSE188792). All other data needed to evaluate the conclusions of the paper are available in the paper or the Supplementary Materials. SARS-CoV-2 stabilized spike glycoprotein was made available from University of Washington through a material transfer agreement. Reagents required for integrating the NEBNext® Single Cell/Low Input cDNA Synthesis & Amplification Module and NEBNext® Immune Sequencing Kit were made available under a material transfer agreement from New England Biolabs. This work is licensed under a Creative Commons Attribution 4.0 International (CC BY 4.0) license, which permits unrestricted use, distribution, and reproduction in any medium, provided the original work is properly cited. To view a copy of this license, visit https://creativecommons.org/licenses/by/4.0/. This license does not apply to figures/photos/artwork or other content included in the article that is credited to a third party; obtain authorization from the rights holder before using this material.

Submitted 21 July 2021
Accepted 14 December 2021
Published First Release 16 December 2021
10.1126/sciimmunol.abl5652

Downloaded from https://www.science.org at University of Massachusetts Worcester on January 12, 2022

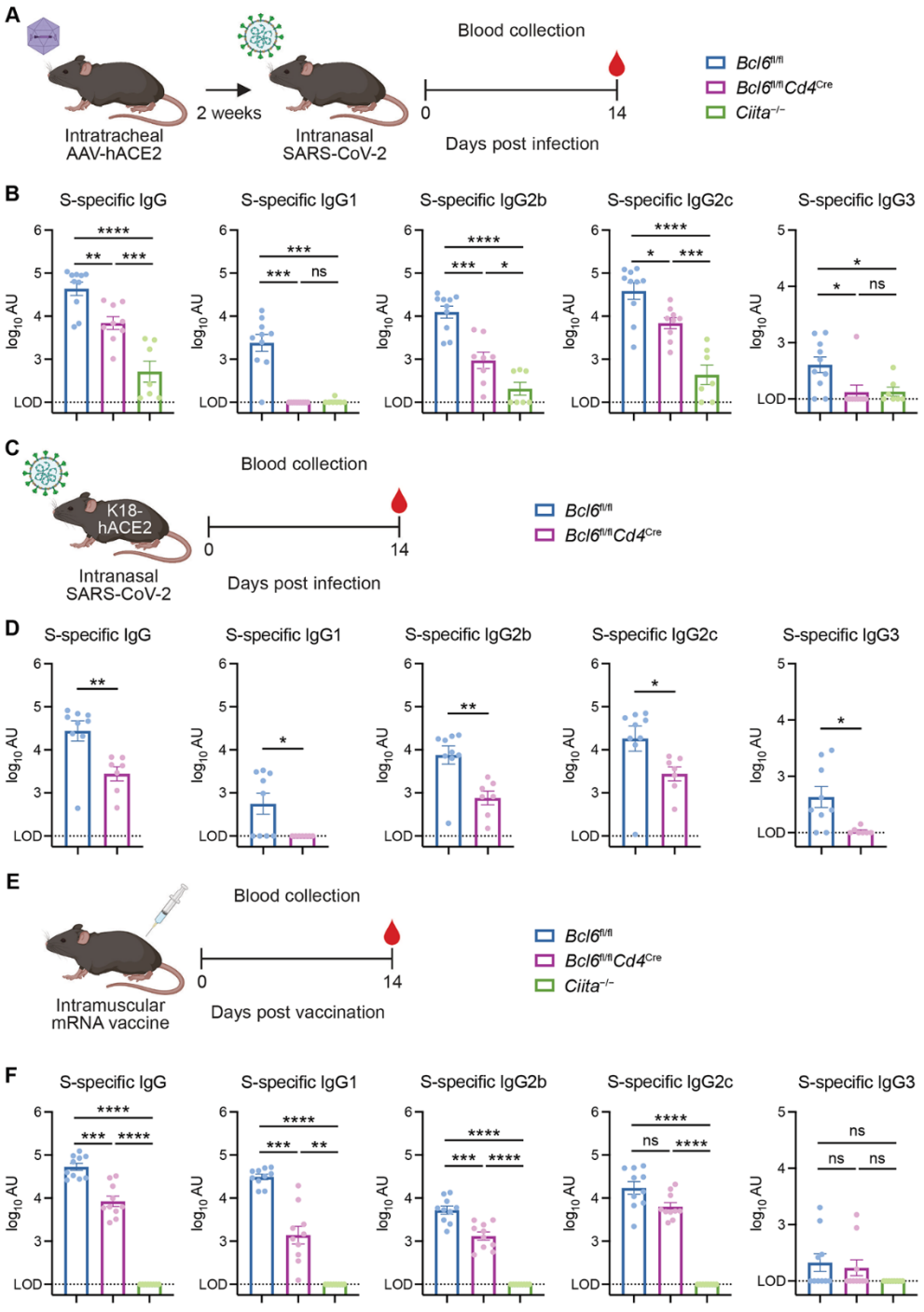

Fig. 1. SARS-CoV-2 infection and vaccination induce Tfh-dependent and -independent antibodies. (**A**) Schematic of experimental design for assessing serum antibody responses against SARS-CoV-2 in AAV-hACE2 mice. Mice were infected intranasally with SARS-CoV-2 (isolate USA-WA1/2020) two weeks following intratracheal administration of AAV-hACE2. Sera were collected 14 days post infection (dpi) for quantification of antibody titers by ELISA. (**B**) Spike (S)-specific total IgG, IgG1, IgG2b, IgG2c, and IgG3 antibody titers in sera from control (*Bcl6*$^{fl/fl}$; blue symbol), Tfh-deficient (*Bcl6*$^{fl/fl}$*Cd4*^{Cre}; magenta symbol), or CD4^{+} T cell-deficient (*Ciita*$^{-/-}$; green symbol) mice at 14 dpi with SARS-CoV-2. (**C**) Schematic of experimental design for assessing serum antibody responses against SARS-CoV-2 in K18-hACE2 mice. Mice were infected with SARS-CoV-2 (isolate USA-WA1/2020) by intranasal administration. Sera were collected at 14 dpi for quantification of antibody titers by ELISA. (**D**) S-specific total IgG, IgG1, IgG2b, IgG2c, and IgG3 antibody titers in sera from K18-hACE2 *Bcl6*$^{fl/fl}$ (blue) or K18-hACE2 *Bcl6*$^{fl/fl}$*Cd4*^{Cre} (magenta) mice at 14 dpi with SARS-CoV-2. (**E**) Schematic of experimental design for assessing serum antibody responses against SARS-CoV-2 mRNA vaccination. Mice were vaccinated intramuscularly with Moderna mRNA-1273 or Pfizer-BioNTech BNT162b2 mRNA vaccine. Sera were collected 14 days post vaccination (dpv) for quantification of antibody titers by ELISA. (**F**) S-specific total IgG, IgG1, IgG2b, IgG2c, and IgG3 antibody titers in sera from *Bcl6*$^{fl/fl}$ (blue), *Bcl6*$^{fl/fl}$*Cd4*^{Cre} (magenta), or *Ciita*$^{-/-}$ (green) mice at 14 dpv with mRNA vaccine. LOD, limit of detection of the assay. Statistical significance was assessed by one-way ANOVA with Tukey's test, or Welch's *t* test with Bonferroni multiple hypothesis correction when sample variances were 0 (B and F); two-tailed unpaired *t* test or Welch's *t* test, based on the F test for unequal variance (D). *$P < 0.05$; **$P < 0.01$; ***$P < 0.001$; ****$P < 0.0001$. ns, not significant. Data are expressed as mean ± standard error of mean (SEM) $\log_{10}$ arbitrary units (AU). Each symbol represents an individual mouse. Data are aggregated from at least two independent experiments with a total of seven to ten mice per condition.

Downloaded from https://www.science.org at University of Massachusetts Worcester on January 12, 2022

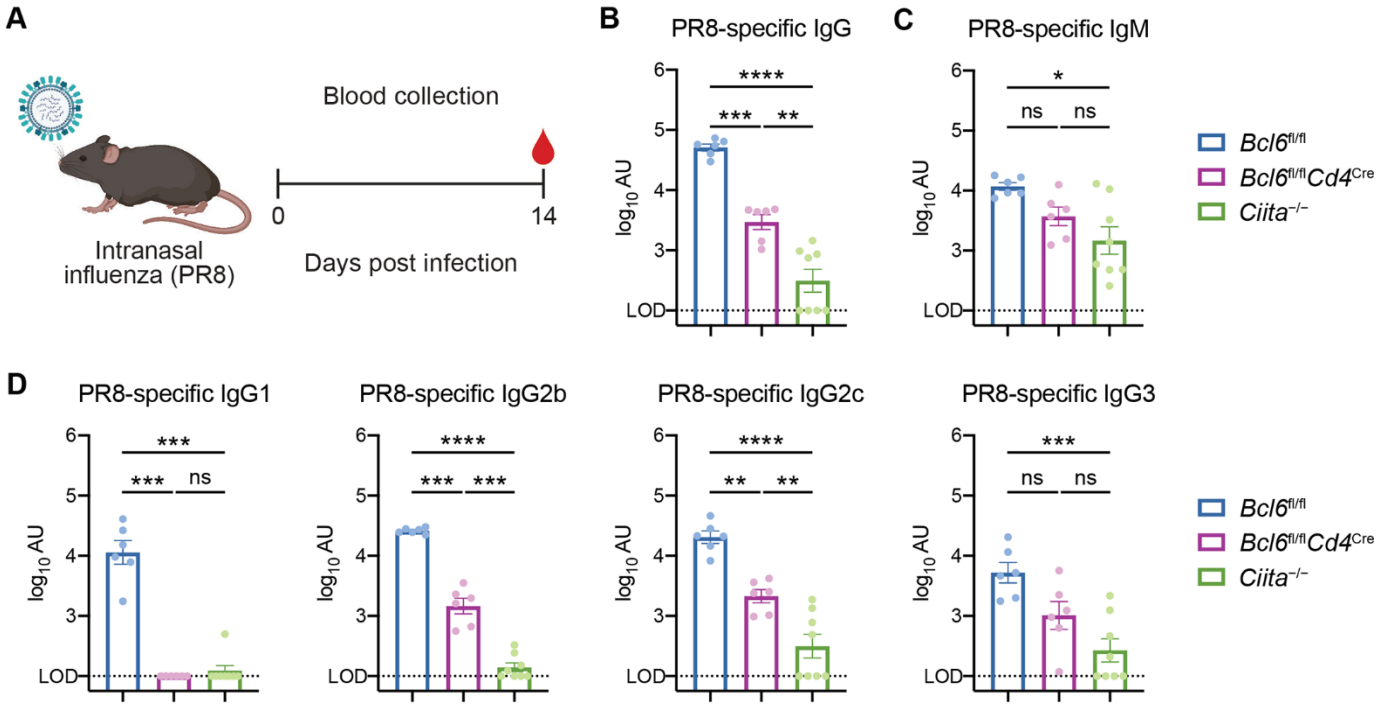

Fig. 2. Influenza virus infection induces Tfh-dependent and -independent antibodies. (**A**) Schematic of experimental design for assessing serum antibody responses against influenza virus. Mice were infected with mouse-adapted influenza virus (PR8) by intranasal administration. Sera were collected at 14 dpi for quantification of antibody titers by ELISA. (**B** and **C**) PR8-specific total IgG (B) and IgM (C) antibody titers in sera from *Bcl6*$^{fl/fl}$ (blue), *Bcl6*$^{fl/fl}$*Cd4*^{Cre} (magenta), or *Ciita*$^{-/-}$ (green) mice at 14 dpi with PR8. (**D**) PR8-specific IgG1, IgG2b, IgG2c, and IgG3 antibody titers at 14 dpi with PR8. LOD, limit of detection of the assay. Statistical significance was assessed by one-way ANOVA with Tukey's test or Dunnett's test, or Welch's *t* test with Bonferroni multiple hypothesis correction when sample variances were 0 (B to D). *$P < 0.05$; **$P < 0.01$; ***$P < 0.001$; ****$P < 0.0001$. ns, not significant. Data are expressed as mean ± SEM $\log_{10}$ arbitrary units (AU). Each symbol represents an individual mouse. Data are aggregated from two independent experiments with a total of six to eight mice per condition.

Downloaded from https://www.science.org at University of Massachusetts Worcester on January 12, 2022

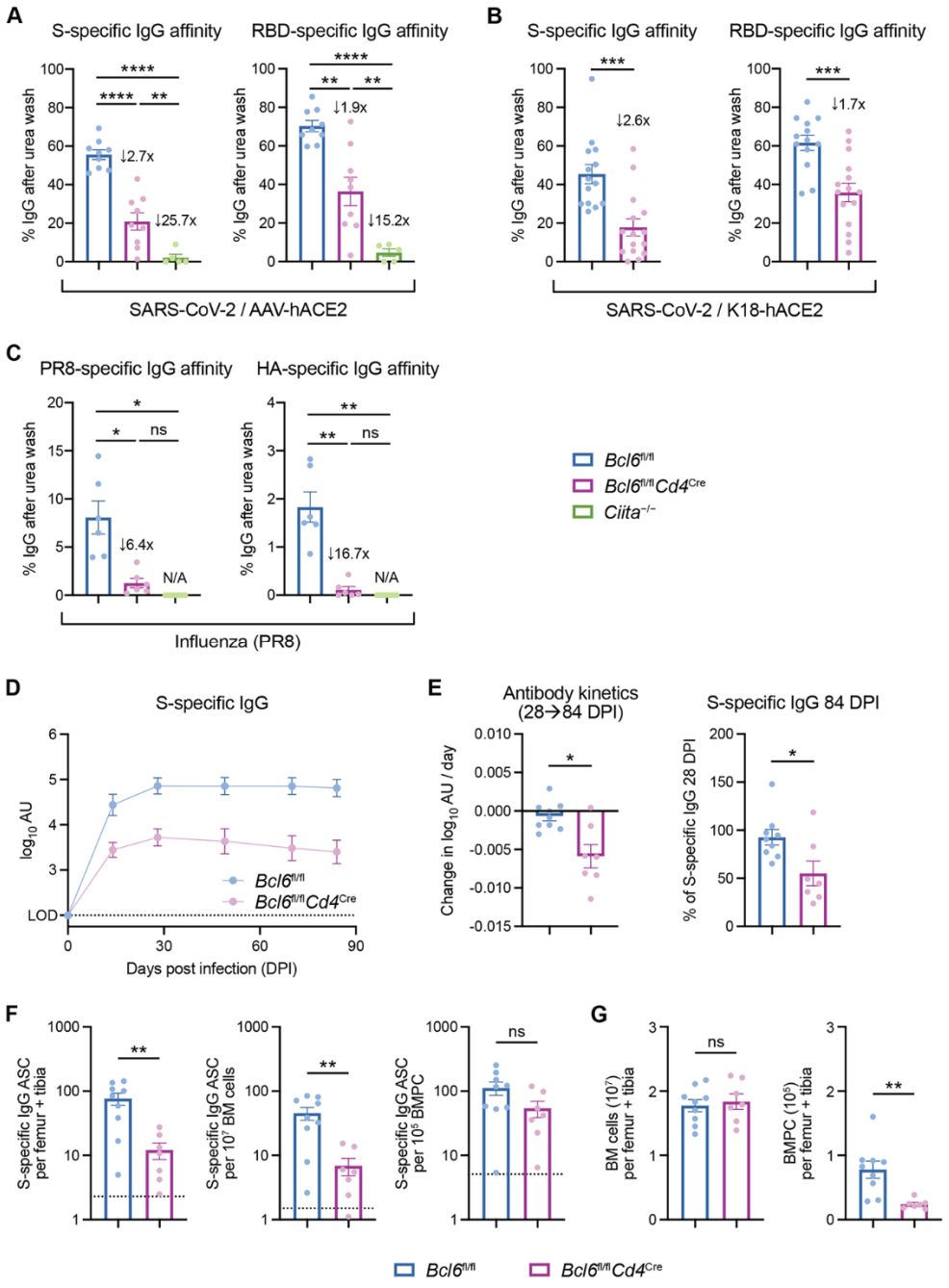

Fig. 3. Durable, high-affinity antibodies to SARS-CoV-2 can be made in the absence of Tfh cells. (**A**) Affinity index of serum IgG antibodies against SARS-CoV-2 S (left) or RBD (right), calculated as relative ELISA signal after urea wash. Sera are from AAV-hACE2 *Bcl6*$^{fl/fl}$ (blue), *Bcl6*$^{fl/fl}$*Cd4*^{Cre} (magenta), or *Ciita*$^{-/-}$ (green) mice infected with SARS-CoV-2 at 14 dpi. Fold changes relative to *Bcl6*$^{fl/fl}$ mice are annotated. (**B**) Affinity index of serum IgG antibodies against SARS-CoV-2 S (left) or RBD (right). Sera are from K18-hACE2 *Bcl6*$^{fl/fl}$ (blue) or K18-hACE2 *Bcl6*$^{fl/fl}$*Cd4*^{Cre} (magenta) mice infected with SARS-CoV-2 at 14 dpi. Fold changes relative to K18-hACE2 *Bcl6*$^{fl/fl}$ mice are annotated. (**C**) Affinity index of serum IgG antibodies against PR8 (left) or HA (right), calculated as relative ELISA signal after urea wash. Sera are from *Bcl6*$^{fl/fl}$ (blue), *Bcl6*$^{fl/fl}$*Cd4*^{Cre} (magenta), or *Ciita*$^{-/-}$ (green) mice infected with PR8 at 14 dpi. Fold changes relative to *Bcl6*$^{fl/fl}$ mice are annotated. (**D**) Longitudinal dynamics of S-specific IgG antibodies up to 84 dpi, in sera from K18-hACE2 *Bcl6*$^{fl/fl}$ or K18-hACE2 *Bcl6*$^{fl/fl}$*Cd4*^{Cre} mice infected with SARS-CoV-2. (**E**) Change in S-specific IgG antibody titer per day between 28 and 84 dpi, as determined by linear regression (left). Relative titers of S-specific IgG at 84 dpi, compared to S-specific IgG at 28 dpi (right). (**F**) ELISpot quantification of S-specific IgG antibody-secreting cells (ASC) in the bone marrow of K18-hACE2 *Bcl6*$^{fl/fl}$ or K18-hACE2 *Bcl6*$^{fl/fl}$*Cd4*^{Cre} mice at 85 dpi with SARS-CoV-2. S-specific IgG ASC per femur + tibia (left), per 10^7 bone marrow (BM) cells (middle), or per 10^5 CD138$^+$ bone marrow plasma cells (BMPC) (right). Dotted line indicates background signal from naïve mice. (**G**) Total number of BM cells (left) and CD138$^+$ BMPC (right) in femur + tibia of K18-hACE2 *Bcl6*$^{fl/fl}$ or K18-hACE2 *Bcl6*$^{fl/fl}$*Cd4*^{Cre} mice at 85 dpi with SARS-CoV-2. Statistical significance was assessed by one-way ANOVA with Dunnett's test, or Welch's *t* test with Bonferroni multiple hypothesis correction when sample variances were 0 (A and C); two-tailed unpaired *t* test or Welch's *t* test, based on the F test for unequal variance (B, E, G); two-tailed Mann–Whitney test (F). $*P < 0.05$; $**P < 0.01$; $***P < 0.001$; $****P < 0.0001$. ns, not significant. Data are expressed as mean ± SEM. Each symbol in (A to C and E to G) represents an individual mouse. Each symbol in (D) represents the mean of nine (*Bcl6*$^{fl/fl}$) and seven (*Bcl6*$^{fl/fl}$*Cd4*^{Cre}) mice. Data are aggregated from at least two independent experiments with a total of five to fifteen mice per condition.

Downloaded from https://www.science.org at University of Massachusetts Worcester on January 12, 2022

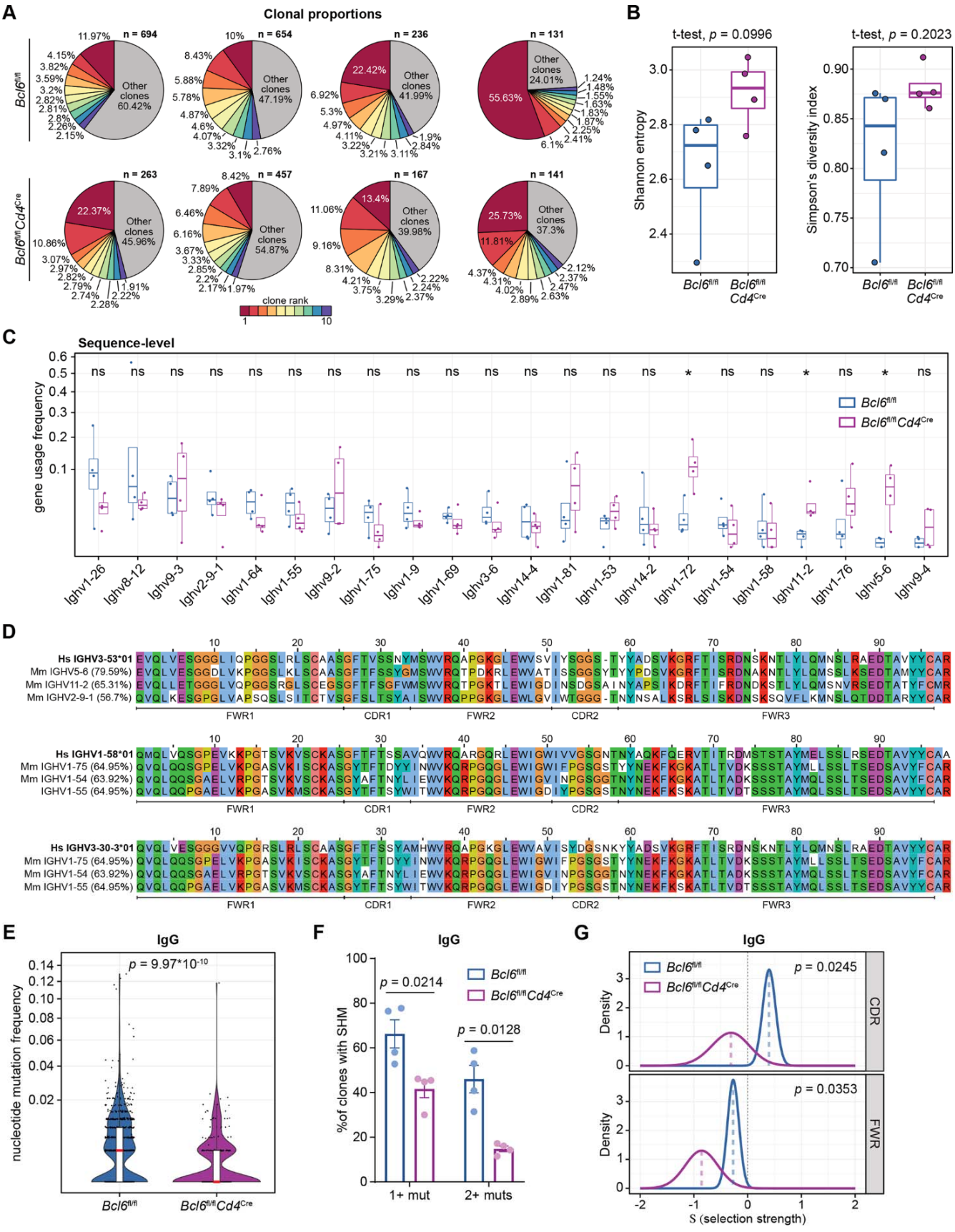

Downloaded from https://www.science.org at University of Massachusetts Worcester on January 12, 2022

Fig. 4. Tfh-deficient mice demonstrate similar V gene usage but impaired mutation selection compared to Tfh-sufficient mice. (**A**) Pie charts detailing the relative proportions of B cell clones identified in K18-hACE2 *Bcl6*$^{fl/fl}$ (top row) or K18-hACE2 *Bcl6*$^{fl/fl}$*Cd4*^{Cre} (bottom row) mice infected with SARS-CoV-2 (n = 4 mice per condition from one experiment). The 10 largest clones in each sample are shown individually, with all other clones grouped together. The total number of clones in each sample is annotated above each pie chart. (**B**) Tukey boxplots detailing Shannon entropy (left) and Simpson's diversity index (right) in *Bcl6*$^{fl/fl}$ or *Bcl6*$^{fl/fl}$*Cd4*^{Cre} mice. Statistical significance was assessed by two-tailed unpaired Welch's t test. Each symbol represents an individual mouse BCR repertoire. (**C**) Tukey boxplots detailing V gene usage frequencies, calculated on the level of total BCR sequences in each sample. V genes with ≥ 0.02 usage frequency in ≥ 2 samples are shown here. Statistical significance was assessed by two-tailed unpaired Mann-Whitney test. *P < 0.05. ns, not significant. (**D**) Alignment of human IGHV3-53, IGHV1-58, IGHV3-30-3 segments to the 3 murine V segments shown in (C) with the highest homology to each of the human V segments. The percentage sequence identity relative to the corresponding human V gene (bolded) is indicated on the left. The FWR and CDR regions within the V segments are annotated below. (**E**) Violin plots of nucleotide mutation frequencies in IgG-predominant B cell clones from *Bcl6*$^{fl/fl}$ or *Bcl6*$^{fl/fl}$*Cd4*^{Cre} mice. Red lines indicate median nucleotide mutation frequency. Statistical significance was assessed by two-tailed unpaired Mann-Whitney test. (**F**) Quantification of the percentage of IgG-predominant B cell clones with either 1+ or 2+ mutations in *Bcl6*$^{fl/fl}$ or *Bcl6*$^{fl/fl}$*Cd4*^{Cre} mice. Statistical significance was assessed by two-tailed unpaired Welch's t test. Data are expressed as mean ± SEM. (**G**) Probability density function curves of selection strength in IgG-predominant B cell clones from *Bcl6*$^{fl/fl}$ or *Bcl6*$^{fl/fl}$*Cd4*^{Cre} mice, as determined by BASELINe analysis. The density curves are separated by region within the V segment: CDRs (top) or FWRs (bottom). Selection was estimated using BASELINe focused test. Statistical differences between the probability density functions were assessed by a two-sample significance test with numerical integration.

Downloaded from https://www.science.org at University of Massachusetts Worcester on January 12, 2022

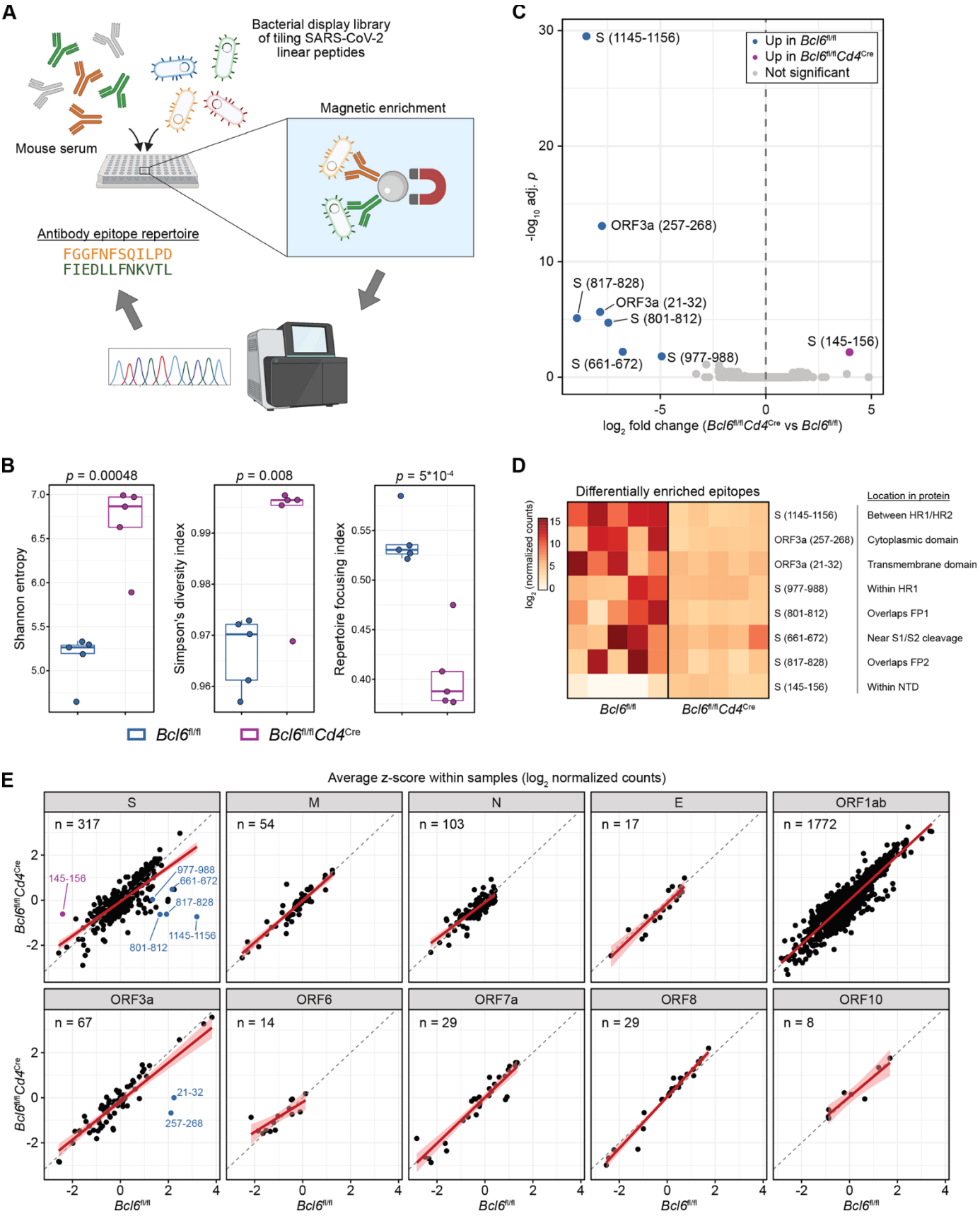

Downloaded from https://www.science.org at University of Massachusetts Worcester on January 12, 2022

Fig. 5. Tfh cells focus the antibody repertoire but are dispensable for broad coverage of SARS-CoV-2 epitopes. (**A**) Sera from infected AAV-hACE2 *Bcl6*$^{fl/fl}$ or *Bcl6*$^{fl/fl}$*Cd4*^{Cre} mice (n = 5 mice per condition from two independent experiments) were assayed for reactivity against a bacterial display library of overlapping linear epitopes tiling the SARS-CoV-2 proteome. (**B**) Tukey boxplots detailing Shannon entropy (left), Simpson's diversity index (middle), and repertoire focusing index (right) in *Bcl6*$^{fl/fl}$ or *Bcl6*$^{fl/fl}$*Cd4*^{Cre} mice. Statistical significance was assessed by two-tailed unpaired Welch's t test. Each symbol represents an individual mouse. (**C**) Volcano plot of differentially enriched linear epitopes in *Bcl6*$^{fl/fl}$ vs *Bcl6*$^{fl/fl}$*Cd4*^{Cre} mice. Epitopes that are significantly enriched in *Bcl6*$^{fl/fl}$ sera are colored in blue, while epitopes that are enriched in *Bcl6*$^{fl/fl}$*Cd4*^{Cre} sera are colored in magenta. Point labels describe the amino acids within the indicated SARS-CoV-2 protein from which the epitope was derived. Statistical significance was assessed by two-tailed DESeq2 Wald test, with Benjamini-Hochberg multiple hypothesis correction (adjusted $p < 0.05$). (**D**) Heatmap of differentially enriched linear epitopes in *Bcl6*$^{fl/fl}$ vs *Bcl6*$^{fl/fl}$*Cd4*^{Cre} mice, from (C). Data are expressed as $\log_2$-transformed normalized counts. The position of each epitope in relation to known protein domains is annotated. (**E**) Scatter plots of relative enrichment scores for linear epitopes derived from each SARS-CoV-2 protein, comparing *Bcl6*$^{fl/fl}$ vs *Bcl6*$^{fl/fl}$*Cd4*^{Cre} sera. Data are expressed as average z-scores ($\log_2$ normalized counts were scaled to z-scores within each sample, then averaged across *Bcl6*$^{fl/fl}$ or *Bcl6*$^{fl/fl}$*Cd4*^{Cre} mice). The gray dashed line demarcates equivalence between *Bcl6*$^{fl/fl}$ and *Bcl6*$^{fl/fl}$*Cd4*^{Cre}, while the red line denotes the linear regression model with 95% confidence intervals shaded in pink. Epitopes that were identified as differentially enriched are annotated as in (C). The number of epitopes derived from each SARS-CoV-2 protein is annotated in the top left.

Downloaded from https://www.science.org at University of Massachusetts Worcester on January 12, 2022

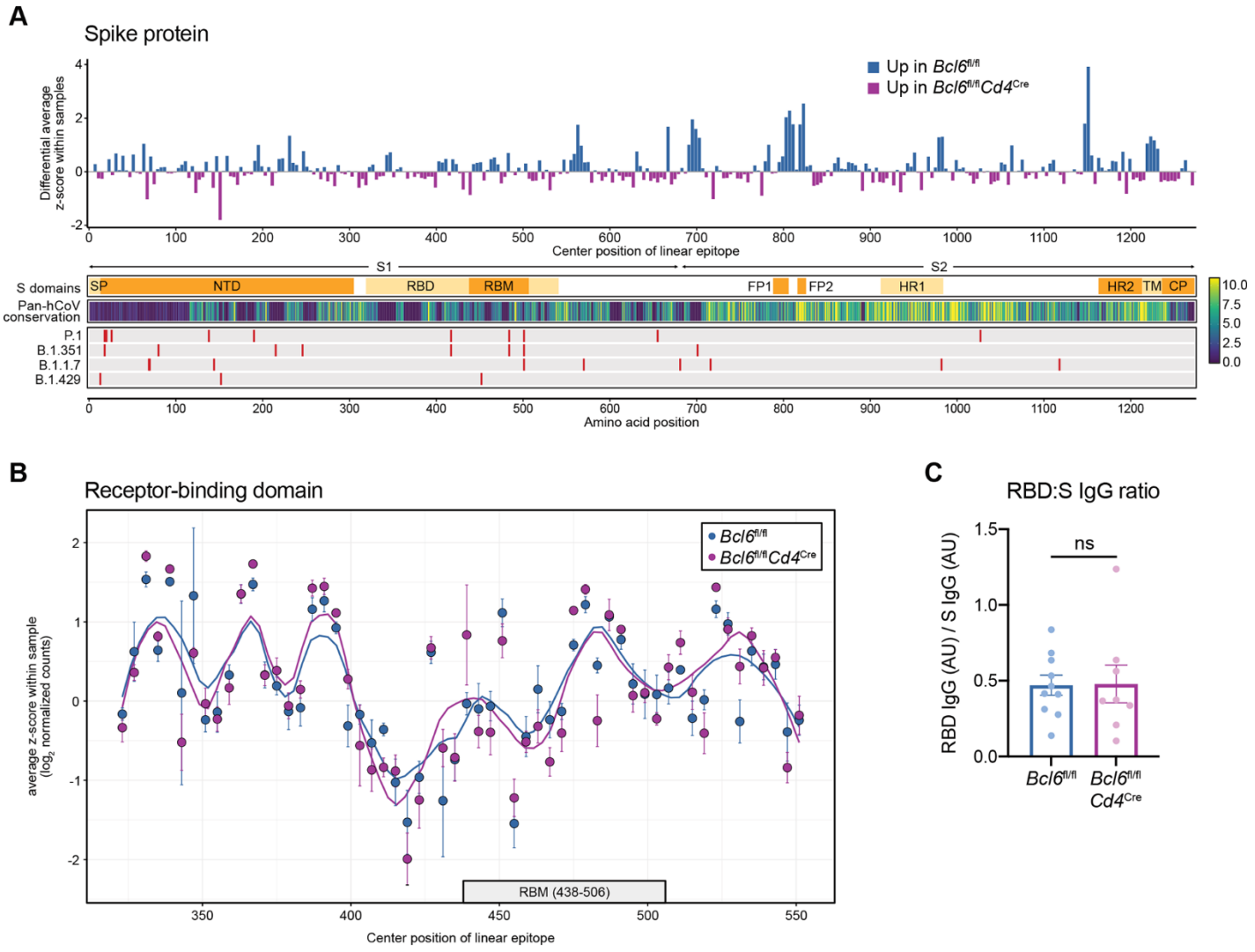

Fig. 6. RBD-specific antibodies are generated in the absence of Tfh cells. (**A**) Top: differential enrichment scores for spike (S)-derived linear epitopes, such that epitopes that are comparatively enriched in *Bcl6*$^{fl/fl}$ mice are represented by positive values (blue), whereas epitopes that are relatively enriched in *Bcl6*$^{fl/fl}$*Cd4*^{Cre} mice are indicated by negative values (magenta). Linear epitopes are each indicated by their center position within the S protein. Bottom: annotation tracks detailing S protein domains, pan-human coronavirus (hCoV) conservation scores, and mutations found in select SARS-CoV-2 variants of concern. SP, signal peptide. NTD, N-terminal domain. RBD, receptor-binding domain. RBM, receptor-binding motif. FP1, fusion peptide 1. FP2, fusion peptide 2. HR1, heptad repeat 1. HR2, heptad repeat 2. TM, transmembrane domain. CP, cytoplasmic domain. (**B**) Relative enrichment scores for linear epitopes derived from RBD, comparing *Bcl6*$^{fl/fl}$ vs *Bcl6*$^{fl/fl}$*Cd4*^{Cre} sera. Data are expressed as average *z*-scores in *Bcl6*$^{fl/fl}$ or *Bcl6*$^{fl/fl}$*Cd4*^{Cre} mice, with SEM error bars and loess regression lines. The RBM is annotated below with a gray box. (**C**) Ratio of RBD-specific to S-specific IgG antibodies in sera from *Bcl6*$^{fl/fl}$ or *Bcl6*$^{fl/fl}$*Cd4*^{Cre} mice at 14 dpi with SARS-CoV-2. Statistical significance was assessed by two-tailed unpaired *t* test. ns, not significant. Data are expressed as mean ± SEM. Each symbol represents an individual mouse. Data are aggregated from three independent experiments with a total of eight to ten mice per condition.

Downloaded from https://www.science.org at University of Massachusetts Worcester on January 12, 2022

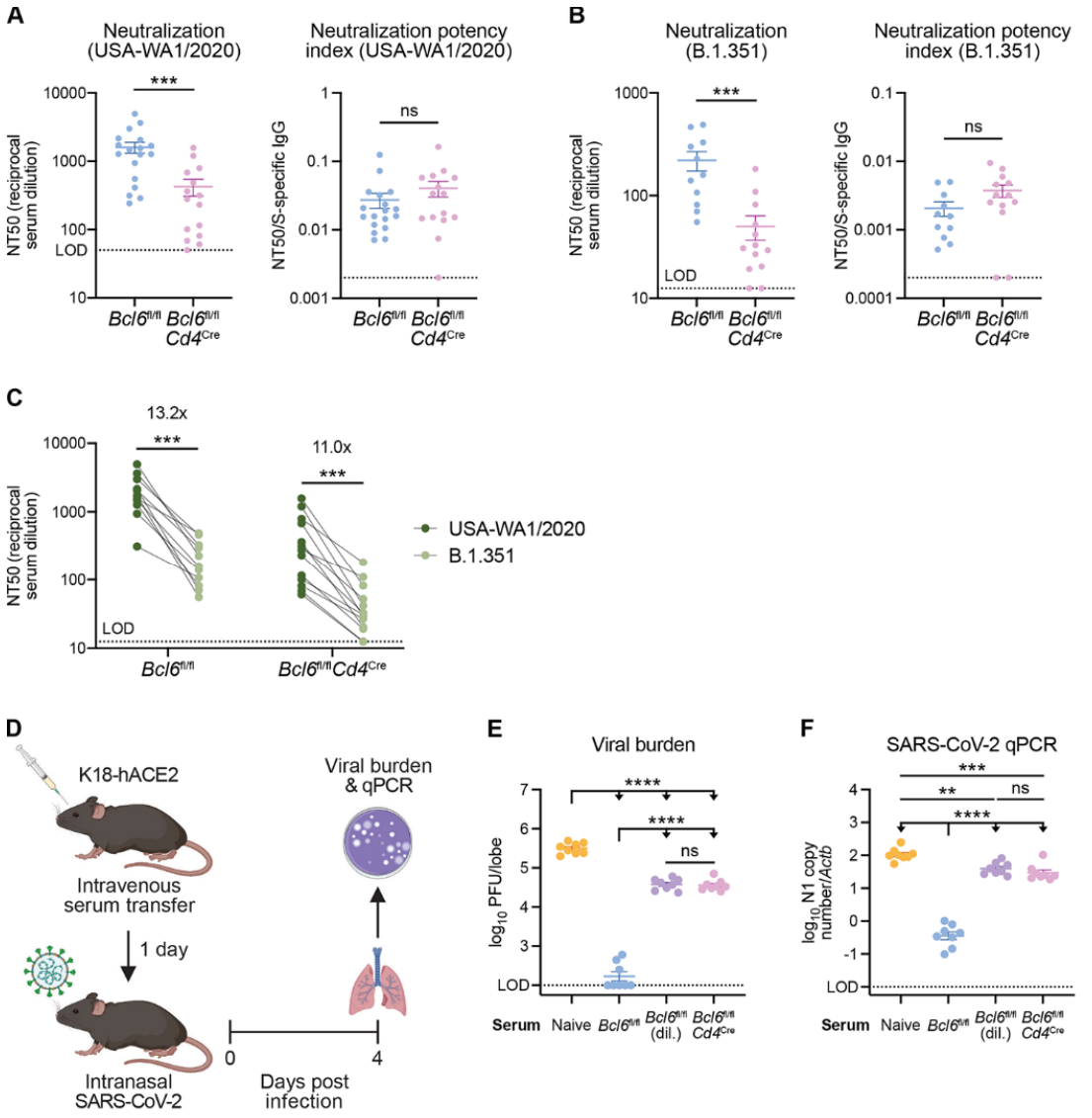

Fig. 7. Tfh-dependent and -independent antibodies demonstrate similar neutralization potency against homologous SARS-CoV-2 as well as the B.1.351 variant of concern. (**A**) Left: neutralizing titers (inverse of half maximal inhibitory concentration; NT50) of sera from AAV-hACE2 *Bcl6*$^{fl/fl}$ (blue) or *Bcl6*$^{fl/fl}$*Cd4*^{Cre} (magenta) mice against VSV particles pseudotyped with homologous S protein (USA-WA1/2020, the same isolate used to infect the mice). Right: neutralization potency indices (NT50 divided by S-specific total IgG) of sera from *Bcl6*$^{fl/fl}$ or *Bcl6*$^{fl/fl}$*Cd4*^{Cre} mice against USA-WA1/2020 pseudovirus. Samples with NT50 at the limit of detection (LOD) were assigned a neutralization potency index of 0.002. (**B**) Left: neutralizing titers of sera from AAV-hACE2 *Bcl6*$^{fl/fl}$ (blue) or *Bcl6*$^{fl/fl}$*Cd4*^{Cre} (magenta) mice against VSV particles pseudotyped with variant S protein (B.1.351). Right: neutralization potency indices of sera from *Bcl6*$^{fl/fl}$ or *Bcl6*$^{fl/fl}$*Cd4*^{Cre} mice against B.1.351 pseudovirus. Samples with NT50 at the LOD were assigned a neutralization potency index of 0.0002. (**C**) Matched comparison of neutralizing titers against homologous (USA-WA1/2020) vs variant (B.1.351) pseudovirus. Fold changes are indicated above each group. (**D**) Schematic of experimental design for assessing in vivo neutralization potency of sera. (**E** and **F**) Viral burden in lungs from K18-hACE2 mice infected with SARS-CoV-2 at 4 dpi. Mice were treated with serum from naïve, infected AAV-hACE2 *Bcl6*$^{fl/fl}$, or infected AAV-hACE2 *Bcl6*$^{fl/fl}$*Cd4*^{Cre} mice. *Bcl6*$^{fl/fl}$ sera was given undiluted or diluted (dil.) 7- to 9-fold to match the S-specific IgG titer of *Bcl6*$^{fl/fl}$*Cd4*^{Cre} sera in each experiment. Data are expressed as $\log_{10}$ plaque forming units (PFU) per lung lobe by plaque assay (E) or $\log_{10}$ N1 gene copy number by qPCR, normalized to *Actb* (F). Statistical significance was assessed by two-tailed Mann–Whitney test (A and B), two-tailed Wilcoxon signed-rank test (C), or one-way ANOVA with Tukey's test (E and F). $^{**}P < 0.01$; $^{***}P < 0.001$; $^{****}P < 0.0001$. ns, not significant. Data are expressed as mean ± SEM. Each symbol represents an individual mouse. Data are aggregated from at least two independent experiments with a total of eight to eighteen mice per condition.

Downloaded from https://www.science.org at University of Massachusetts Worcester on January 12, 2022

Science Immunology

High-affinity, neutralizing antibodies to SARS-CoV-2 can be made without T follicular helper cells

Jennifer S. ChenRyan D. ChowEric SongTianyang MaoBenjamin IsraelowKathy KamathJoel BozekowskiWinston A. HaynesRenata B. FillerBridget L. MenascheJin WeiMia Madel AlfajaroWenzhi SongLei PengLauren CarterJason S. WeinsteinUthaman GowthamanSidi ChenJoe CraftJohn C. ShonAkiko IwasakiCraig B. WilenStephanie C. Eisenbarth

Sci. Immunol., **Ahead of Print**

View the article online
https://www.science.org/doi/10.1126/sciimmunol.abl5652
Permissions
https://www.science.org/help/reprints-and-permissions

Downloaded from https://www.science.org at University of Massachusetts Worcester on January 12, 2022

Use of think article is subject to the Terms of service

Science Immunology (ISSN) is published by the American Association for the Advancement of Science. 1200 New York Avenue NW, Washington, DC 20005. The title *Science Immunology* is a registered trademark of AAAS.
Copyright © 2021, American Association for the Advancement of Science